AGU PUBLICATIONS

JGR

Journal of Geophysical Research: Space Physics

RESEARCH ARTICLE

10.1002/2017JA024923

**Key Points:**
- The magnetic field distribution, configuration, and current density in Mercury's magnetotail are quantitatively addressed
- Mercury's magnetotail is elongated along the south-north direction, which is probably due to the effect of the dipole offset or the induction effect of core
- The magnetic structure of tail current sheet shows a clear dawn-dusk asymmetry with smaller $B_z$ and less flaring field on the duskside

**Correspondence to:**
Z. J. Rong,
rongzhaojin@mail.iggcas.ac.cn

**Citation:**
Rong, Z. J., Ding, Y., Slavin, J. A., Zhong, J., Poh, G., Sun, W. J., … Shen, C. (2018). The magnetic field structure of Mercury's magnetotail. *Journal of Geophysical Research: Space Physics*, *123*, 548–566. https://doi.org/10.1002/2017JA024923

Received 25 OCT 2017
Accepted 4 JAN 2018
Accepted article online 18 JAN 2018
Published online 29 JAN 2018



# The Magnetic Field Structure of Mercury's Magnetotail

**Z. J. Rong[1,2,3], Y. Ding[1,2], J. A. Slavin[4], J. Zhong[1,3], G. Poh[4], W. J. Sun[1,3], Y. Wei[1,2,3], L. H. Chai[1,2,3], W. X. Wan[1,2,3], and C. Shen[5]**

[1]Key Laboratory of Earth and Planetary Physics, Institute of Geology and Geophysics, Chinese Academy of Sciences, Beijing, China, [2]College of Earth Science, University of Chinese Academy of Sciences, Beijing, China, [3]Institutions of Earth Science, Chinese Academy of Sciences, Beijing, China, [4]Department of Climate and Space Sciences and Engineering, University of Michigan, Ann Arbor, MI, USA, [5]Harbin Institute of Technology, Shenzhen, China

**Abstract** In this study, we use the magnetic field data measured by MErcury Surface, Space ENvironment, GEochemistry, and Ranging from 2011 to 2015 to investigate the average magnetic field morphology of Mercury's magnetotail in the down tail 0–3 $R_M$ ($R_M$ = 2,440 km, Mercury's radius). It is found that Mercury has a terrestrial-like magnetotail; the magnetic field structure beyond 1.5 $R_M$ down tail is stretched significantly with typical lobe field 50 nT. A cross-tail current sheet separating the antiparallel field lines of lobes is present in the equatorial plane. The magnetotail width in north-south direction is about 5 $R_M$, while the transverse width is about 4 $R_M$. Thus, the magnetotail shows elongation along the north-south direction. At the cross-tail current sheet center, the normal component of magnetic field (10–20 nT) is much larger than the cross-tail component. The lobe-field-aligned component of magnetic field over current sheet can be well fitted by Harris sheet model. The curvature radius of field lines at sheet center usually reaches a minimum around midnight (100–200 km) with stronger current density (40–50 nA/m$^2$), while the curvature radius increases toward both flanks (400–600 km) with the decreased current density (about 20 nA/m$^2$). The half-thickness of current sheet around midnight is about 0.25 $R_M$ or 600 km, and the inner edge of current sheet is located at the down tail about 1.5 $R_M$. Our results about the field structure in the near Mercury's tail show an evident dawn-dusk asymmetry as that found in the Earth's magnetotail, but reasons should be different. Possible reasons are discussed.

## 1. Introduction

Mercury, the closest planet to Sun, is the only terrestrial planet other than Earth to possess an intrinsic global magnetic field (Ness et al., 1974, 1975). The earlier measurements from Mariner 10 during its three flybys demonstrated that the interaction of the global dipolar magnetic field with the solar wind creates Mercury's magnetosphere; however, its space environment is still poorly understood (e.g., Fujimoto et al., 2007; Russell et al., 1988; Slavin, 2004). The latest mission to explore Mercury exclusively is the MErcury Surface, Space ENvironment, GEochemistry, and Ranging (MESSENGER) spacecraft (Solomon et al., 2007), which was launched on 3 August 2004. After multiple orbit maneuvers and three flybys to Mercury, MESSENGER was inserted into Mercury orbit on 17 March 2011.The orbit around Mercury was highly eccentric with inclination of 82.5° and period of 12 h. The average perigee altitude was about 200 km and apogee altitude 15,200 km. The orbit period was adjusted to about 8 h on April 2012. The mission ended on 30 April 2015 after MESSENGER exhausted its fuel and crashed into the planet's surface.

One of the main goals of MESSENGER is to explore the dynamics of Mercury's magnetosphere (Slavin et al., 2007). The magnetic field measurements collected by MESSENGER confirm the global dipolar field of Mercury as intrinsic magnetic field and found that its dipole moment is 195 ± 10 nT$R_M^3$ ($R_M$ is Mercury's radius, or 2,440 km). The dipole center has a northward offset from the planet's center by about 0.2 $R_M$, or 484 ± 11 km, and the dipole moment orientation is nearly axially aligned (tilt angle is less than 3°) (Alexeev et al., 2010; Anderson et al., 2011, 2012; Johnson et al., 2012). The dipole moment of Mercury is about 1/1000 of that of Earth (Anderson et al., 2008; Slavin et al., 2008); thus, the interaction of the solar wind with its dipolar magnetic field creates a miniature Earth-like magnetosphere.

The magnetotail, the elongated magnetosphere at the nightside, is an extremely dynamic region, since dynamic activities, e.g., magnetic reconnections and plasma instabilities, occur frequently there (e.g., Baker et al., 1996; Baumjohann et al., 1999; Lui, 2003; Miura, 2001). The MESSENGER magnetic field measurements collected in the Mercury's magnetotail during the three flybys were first analyzed by Slavin et al. (2012). Since

MESSENGER's orbital insertion in 2011, there had been many studies on the magnetic field and plasma structure of Mercury's magnetotail. DiBraccio, Slavin, Raines, et al. (2015) presented the first observation of Mercury's plasma mantle and showed clear proton velocity dispersion, which are characteristic of a plasma mantle. From the velocity dispersion, they also estimate the cross-magnetosphere electric potential to be 23–29 kV, consistent with previous estimates from magnetopause reconnection and tail loading/unloading events (Slavin et al., 2010). Using the plasma measurements from the Fast Imaging Plasma Spectrometer (FIPS) (Andrews et al., 2007), Raines et al. (2013) and Gershman et al. (2014) characterized the plasma ion composition and kinetics of Mercury's plasma sheet. Using both the magnetic field and plasma measurements, Poh et al. (2017a) characterized the structure, properties (e.g., thickness and average current density), and stress balance of Mercury's cross-tail current sheet. By fitting each current sheet with a Harris current sheet model, they concluded that about 73% of the identified current sheet can be well described by the Harris model and that heavy ions are important in maintaining MHD stress balance in Mercury's central plasma sheet. Many Earth-like dynamic characteristics are also found in Mercury's magnetotail, such as the flux ropes or plasmoids (DiBraccio, Slavin, Imber, et al., 2015), Earth-like substorm processes including tail loading-unloading and dipolarization fronts (Slavin et al., 2010; Sun et al., 2015, 2016; Sundberg et al., 2012), and Kelvin-Helmholtz vortices near low-latitude boundary of magnetotail (e.g., Boardsen et al., 2010; Gershman et al., 2015).

To investigate the physics of these dynamic processes of Mercury's magneotail, the knowledge of the average magnetic field distribution in magnetotail is very necessary, though some Mercury's magnetospheric models are available (e.g., Alexeev et al., 2008, 2010; Johnson et al., 2012; Korth et al., 2015). The magnetic field observations of the magnetotail taken by MESSENGER over its 5 year orbital phase provide an outstanding opportunity to explore the global magnetic field structure of this planetary magnetotail. The highly eccentric orbit of MESSENGER covered the magnetotail to downtail distances up to about 4 $R_M$. However, only the southern hemisphere of magnetotail was fully covered due to the bias of orbit introduced by the high latitude of periapsis, i.e., about 60° at north latitude (Slavin et al., 2007).

Recently, Poh et al. (2017b) utilized 319 current sheet crossing events to focus on the magnetic field distribution properties in the sheet center. Being different from Poh et al. (2017b), with the magnetic field data of MESSENGER during the entire orbiting period (March 2011 to April 2015), this study aims to derive the average magnetic field morphology of Mercury's magnetotail. To simplify the study, the upstream solar wind conditions (it includes the orientation of interplanetary magnetic field (IMF) and the dynamic pressure of solar wind), the substorm processes, and the induction effect of core (Glassmeier et al., 2007; Johnson et al., 2016; Slavin et al., 2014; Zhong, Wan, Wei, et al., 2015) are not considered. According to the derived magnetic field distribution, we also quantitatively estimate the average curvature radius of magnetic field and the current density at the center of tail current sheet. The implications of the derived results are discussed with the comparison of Earth's magnetotail.

## 2. Data Set

The magnetometer (MAG) onboard MESSENGER can provide the measurement of the magnetic field vector (Anderson et al., 2007). MAG is a low-noise, triaxial, fluxgate instrument with its sensor mounted on a 3.6 m long boom. MAG has a coarse range, ±51,300 nT full scale (1.6 nT resolution), for preflight testing, and a fine range, ±1,530 nT full scale (0.047 nT resolution), for Mercury operation. Using the selectable filter and subsampling techniques, MAG can provide output sample rates from 0.01 $s^{-1}$ to 20 $s^{-1}$. To minimize the noise and high-frequency fluctuations, we use the MAG data with reduced time resolution (1 min) in this study to draw the average magnetic field distribution of magnetotail. In other words, any variations shorter than the fast Dungey cycle (period is 1–2 min) (e.g., Slavin et al., 2010) cannot be resolved by this study. The used data set covers the whole orbiting period from 23 March 2011 to 30 April 2015.

In the following sections the solar wind-aberrated Mercury solar magnetospheric (MSM) coordinates are used unless otherwise stated, where origin is at the dipole center which is shifted northward 0.198 $R_M$ (484 km) from planetary center, $+X$ is antiparallel to upstream solar wind flow, $+Z$ is normal to Mercury's orbital plane and points northward, and $+Y$ complete the right-handed coordinate system. In other words, the aberration effect of Mercury's orbital motion has been considered in this coordinates, where the upstream solar wind

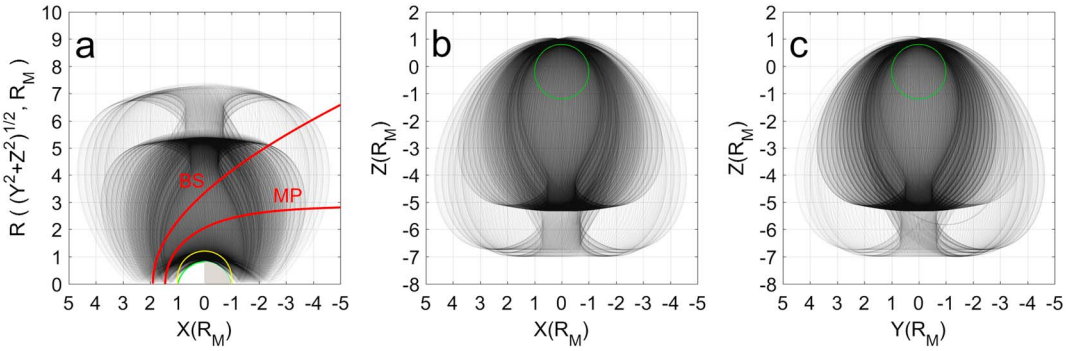


**Figure 1.** Panels from left to right show the MESSENGER's orbits in the plane of (a) *X-R*, (b) *X-Z*, and (c) *Y-Z*, respectively. In Figure 1a, the *Y* label means the distance to the *X* axis. The red curves are the mean locations of the magnetopause (MP) and bow shock (BS) from the models developed by Winslow et al. (2013). The green line and yellow line mark the northern and southern hemispheres of Mercury body, respectively, with nightside being gray-shaded. In Figures 1b and 1c, the green circle represents the Mercury body.

flow is assumed to be a typical average radial speed 400 km/s plus the transverse velocity of Mercury's orbital motion (e.g., Baker et al., 2013; Zhong, Wan, Slavin, et al., 2015).

Figure 1 shows the spatial coverage of MESSENGER's orbit. It is clear from Figure 1a that MESSENGER can detect the magnetotail with downstream distance up to $X \approx -4\ R_M$ and the coverage of plasma sheet ($Z \sim 0$) is only up to $X \approx -3\ R_M$. Figures 1b and 1c demonstrate that the elliptic orbit favors the full coverage of south hemisphere of magnetotail. As a reference in Figure 1a, the red solid lines are the model of magnetopause developed by Winslow et al. (2013) with $R_{ss}$ (subsolar standoff distance) = 1.45 $R_M$ and the shape of Mercury's bow shock with $R_{ss}$ = 1.96 $R_M$. In Figure 1a, the green line and yellow line mark the Mercury body at the northern hemisphere and southern hemisphere, respectively. In both Figures 1b and 1c, the green circle represents the Mercury body.

To characterize the regions of Mercury's magnetosphere, it is helpful to check the distribution of magnetic field data at the beginning of this study. Figure 2 shows the spatial distribution of magnetic field strength observed by MESSENGER around Mercury. To produce Figure 2, the bin size is adopted as 0.15 × 0.15 $R_M$ (the bin size is used in the following sections unless otherwise stated). All data points of field strength are put into these bins, and for each bin, we compute the average. It is found that the sharp spatial variation of magnetic field strength indicating the location of bow shock and magnetopause can be well fitted by the models of Winslow et al. (2013) with the exception of the tail magnetopause, which is slightly overestimated. One should note that the models of bow shock and magnetopause of Winslow et al. (2013) are assumed to be symmetric about the *X* axis. To survey the general shape of magnetopause, Zhong, Wan, Slavin, et al. (2015) developed a 3-D asymmetric model, which includes an indentation for the cusp region. As a reference, the 3-D asymmetric magnetopause model of Zhong, Wan, Slavin, et al. (2015) with subsolar distance *R*ss = 1.51 $R_M$ is also shown in Figure 2.

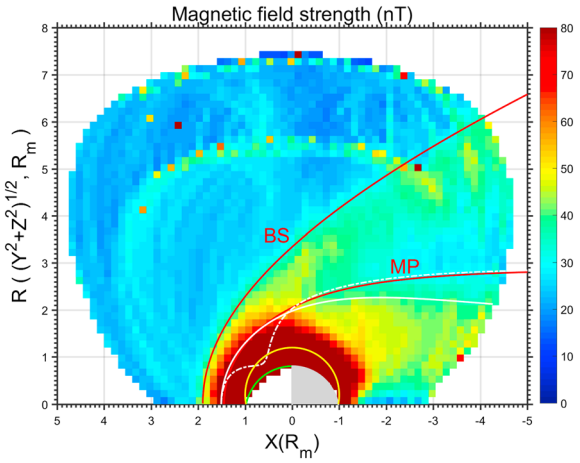


**Figure 2.** The distribution of magnetic field strength observed by MESSENGER around Mercury. The red lines mark the nominal locations of BS and MP as inferred from the models of Winslow et al. (2013). As a comparison, the white solid line and the white dotted line, respectively, representing the MP shape on the equatorial plane ($Z = 0$) and the polar plane ($Y = 0$) are also displayed from the model of Zhong, Wan, Slavin, et al. (2015). The green line and yellow line mark the Mercury body at the northern hemisphere and southern hemisphere, respectively.

In addition, from Figure 2, we notice that the field strength in magneotail lobe is typically about 50 nT at $X < -1.5\ R_M$, while the tail plasma sheet is characterized by the much weaker field at the down tail near $R = 0$.

It is noteworthy that due to the extreme events in solar wind, e.g., interplanetary coronal mass ejection, corotating interaction region, and other structures associated with the enhanced dynamic pressure of solar wind, etc., some dotted bins in Figure 2 show rather high value of magnetic field (>50 nT).

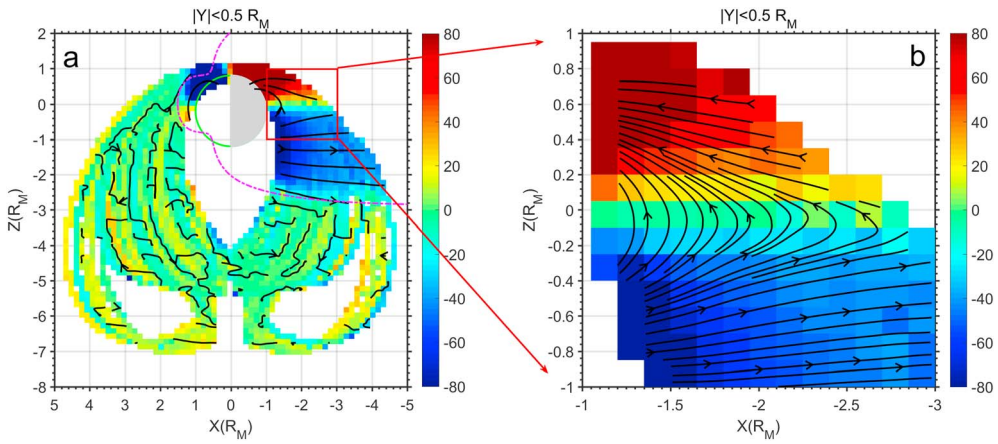


**Figure 3.** (a) A cut of the distribution of $B_x$ component in *X-Z* pane near noon-midnight meridian within $|Y| < 0.5\ R_M$, where the magenta dash-dotted line mark the nominal MP on the plane of $Y = 0$ inferred from the model of Zhong, Wan, Slavin, et al. (2015). (b) The distribution when zoomed in the region $|Z| < 1\ R_M$ and $-1 > X > -3\ R_M$. In both panels, the black curves represent the average magnetic field lines.

## 3. Statistical Results

In this section, we will examine the distribution properties of magnetic field in the magnetotail and derive the global magnetic morphology of magnetotail. Meanwhile, the mean field structure and the current density distribution in magnetotail current sheet are also surveyed.

### 3.1. Distribution in *X-Z* Plane

Previous studies show that Mercury has a terrestrial-like, stretched magnetotail (DiBraccio, Slavin, Raines, et al., 2015; Gershman et al., 2014; Slavin et al., 2012), which contains two antiparallel lobes separated by a current sheet (Poh et al., 2017a). To confirm this knowledge, as shown in Figure 3, we take a cut in the *X-Z* plane with $-0.5 < Y < 0.5\ R_M$ ($|Y| < 0.5\ R_M$, near noon-midnight meridian) to survey the magnetic field distribution. To simplify the figure, only the distribution of $B_x$ component is displayed.

Figure 3a shows the average spatial distribution of $B_x$ component. The data points in each bin are averaged. The black curves with arrow representing the average magnetic field lines are also displayed based on the $B_x$ and $B_z$ component distributions ($B_z$ distribution is not shown here). The magnetic field lines are calculated using linear interpolation. Clearly, the field lines are significantly stretched at the wake region, and a transition layer, identified as the tail plasma sheet, separates antiparallel field lines of lobe within $0 > X > -3\ R_M$. The $B_x$ distribution in the southern hemisphere, which is fully covered by the orbit, indicates that the scale of southern hemisphere along *Z* direction is about $2.5\ R_M$.

In the region between $-1 > X > -3\ R_M$ and $|Z| < 1\ R_M$, as shown in Figure 3b, the distribution of $B_x$ component and the field lines' structure can be seen more clearly. From Figure 3b, characteristics of terrestrial-like magnetotail can be found clearly: The $B_x$ component is basically positive at $Z > 0$ while negative at $Z < 0$. The field lines are basically antiparallel in the two hemispheres, like that in the Earth magnetotail lobe regions. The field lines are significantly stretched near $Z = 0$ where a transition layer of $B_x = 0$ is presented. The field lines are stretched significantly, particularly at the downstream when $X < -1.5\ R_M$, which may demonstrate the significant tail current operates significantly there. The study of tail current will be addressed in section 3.4.

### 3.2. Distribution in *Y-Z* Plane

In this section, we investigate the magnetic field distribution in the *Y-Z* plane. To check the possible difference of distribution with the magnetotail downstream distance, the downstream distance is divided into three regions, i.e., $-1.0 > X > -1.5\ R_M$, $-1.5 > X > -2.0\ R_M$, and $-2.0 > X > -2.5\ R_M$.

Figure 4 shows the distribution of the three components of magnetic field vector, i.e., $B_x$, $B_y$, and $B_z$ in the left, middle, and right columns, respectively. The distribution shows the consistent features of tail field

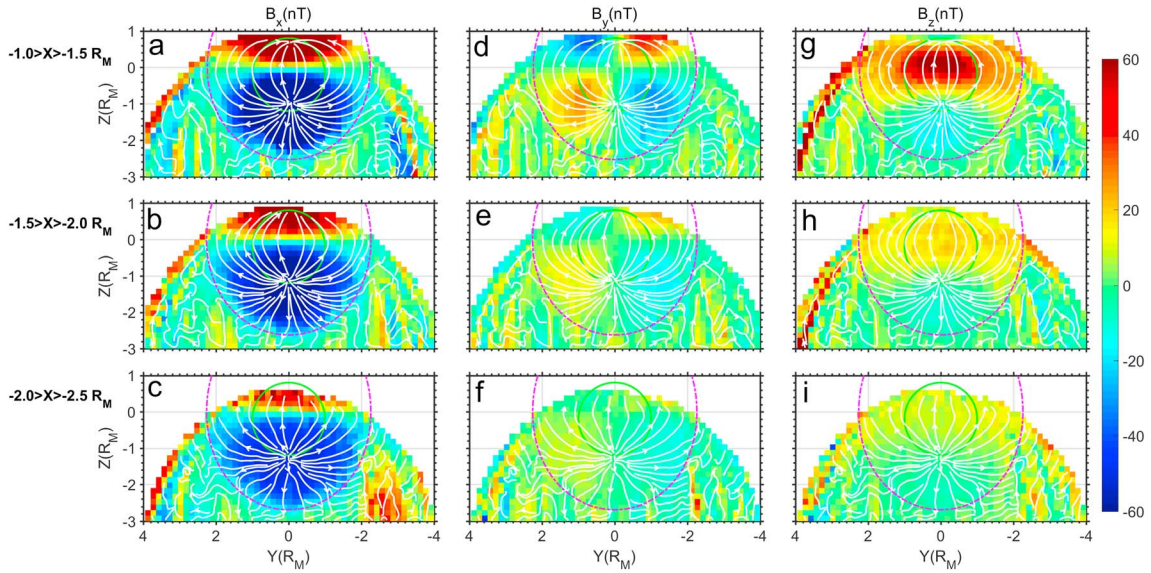


**Figure 4.** (a–i) The distributions of $B_x$, $B_y$, and $B_z$ components in *Y-Z* plane with different down-tail distance, as seen sunward. In these panels, the white lines represent the average magnetic field lines in the corresponding distance scopes; i.e., the field lines in the panels of each row are the same green circle that outlines the shape of Mercury. From top to the bottom, the magenta dash-dotted line marks the nominal magnetopause at $X = -1.25$, 1.75, and 2.25 $R_M$, respectively, as inferred from the model of Zhong, Wan, Slavin, et al. (2015).

configuration as that found in the Earth magnetotail (e.g., Fairfield, 1979; Slavin et al., 1985), e.g., a pair of lobe regions separated by a current sheet (see Figures 4a–4c), the field lines are flaring with respect to $Y = 0$ (see Figures 4d–4f), and the $B_z$ is positive and enhanced around $Z = 0$ (see Figures 4g–4i). Within the magnetotail, the field lines are well ordered that the field lines are emanating from the southern hemisphere and converging into the northern hemisphere, but becomes relatively disordered outside the magnetotail boundary.

Additionally, several interesting features are also noticed from these panels:

1. The whole magnetotail current sheet is basically located at the equatorial plane ($Z = 0$). As well known, at the both flanks of Earth magnetotail current sheet (near the equatorial plane and close to the tail magnetopause), the sheet is warped severely due to the nonnegligible dipole tilt angle (the angle between dipole axis and the planetary spin axis, which is about 11.5° for Earth) (e.g., Tsyganenko & Fairfield, 2004). Nonetheless, the dipole tilt angle of Mercury is less than 0.8° according to the estimation of Anderson et al. (2012); thus, the tail current sheet basically located at the equatorial region is consistent with expectation of the minor dipole tilt angle.
2. The magnetotail is elongated along north-south direction. From Figures 4a–4c, the scale of magnetotail southern hemisphere along Z direction is about 2.5 $R_M$. Thus, with assumption of south-north symmetry, the scale of magnetotail along *Z* direction is about 5 $R_M$, larger than the scale along the *Y* direction (about 4 $R_M$). This feature is consistent with the Mercury's magnetopause model as recently developed by Zhong, Wan, Slavin, et al. (2015), who also find that the nightside magnetopause is elongated along south-north direction.
3. The typical $B_x$ magnitude in lobe is about 50 nT. From Figures 4a–4c, the area of one lobe can be roughly estimated to be $S \approx 2.5\ \pi R_M^2$ (seen as the half of an ellipse whose area is $\pi \times 2\ R_M \times 2.5\ R_M$). Thus, the open magnetic flux of magnetotail can be estimated as $\Phi \approx SB_x \approx 2.3 \times 10^6$ Wb. Since the open magnetic flux is linked to the polar cap, the polar cap latitude can be calculated when considering the dipole moment. Taking account of the previously estimated dipole moment 195 nT × $R_M^3$ (Anderson et al., 2011), the average polar cap latitude is estimated as 37°. If further considering the north shift of 484 km of the dipole center (Anderson et al., 2011), the latitude of the equatorward boundary of Mercury's northern (southern) polar cap is about 40° (about 34°) (see Appendix A for the detailed calculation). Note that, the actual boundary may have large variability and highly day-night asymmetry. Our estimated value of the northern boundary is slightly equatorward than the latitude range of the northern cusp (e.g., Poh et al., 2016;

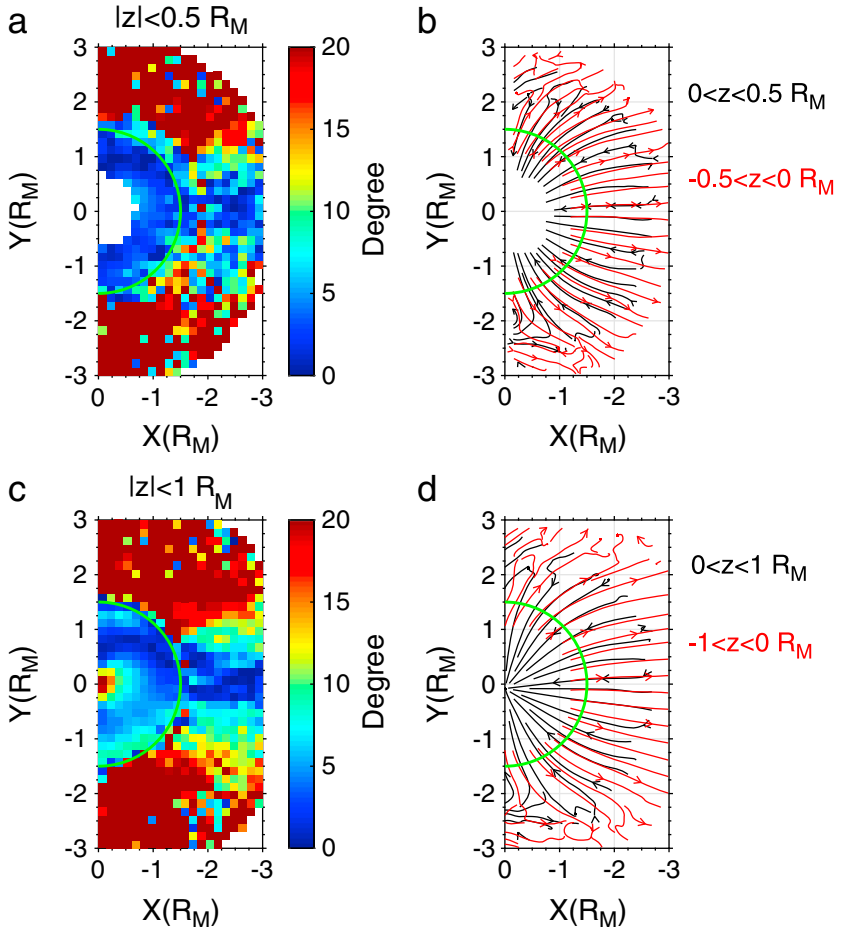


**Figure 5.** (a) The deviation angle of average magnetic field direction from the radial direction when projected onto the *X-Y* plane and (b) the average configuration of magnetic field lines in magnetotail when $|Z| < 0.5\ R_M$. With the same format, (c and d) the deviation angle and the field lines, respectively, was also shown when $|Z| < 1\ R_M$. In these panels, the green hemi-circle with radius 1.5 $R_M$ roughly marks the boundary where field lines are stretched significantly from the dipole field.

Winslow et al., 2012), but basically consistent with the nightside precipitation latitude of planetary $Na^+$ (e.g., Delcourt & Seki, 2006) and the solar wind $H^+$ (Kallio & Janhunen, 2003).

4. From Figures 4g–4i and 3a, near the boundary of southern magnetotail, the magnetotail field lines are directed a bit southward. Accordingly, the magnetopause of southern magnetotail is flaring southward. The deviated angle of the field lines from *X* axis is roughly estimated as 14° at the boundary of the southern magnetotail.

### 3.3. Magnetic Field Configuration in Magnetotail

Based on the distributions of magnetic field addressed in the above subsections, we study the magnetic field configurations in magnetotail in this section.

The magnetic field in Mercury's magnetotail basically consists of two sources if penetrated IMF into magnetosphere (e.g., Petrukovich, 2011; Rong et al., 2015) can be ignored, i.e., the component of the dipole field and the component induced by the magnetospheric current systems. Thus, it is expected that the closer to Mercury the more dipole-like the field configurations become. Since the dipole field has no azimuthal component making the orientations of dipole field radial when projected onto the *X-Y* plane, we can define a deviation angle between the local magnetic field direction and the radial direction to evaluate how much the local field configuration deviated from the dipole field. The deviation angle is calculated as $\Delta\alpha = \left|\mathrm{a\,tan}\left(\left|\frac{Y}{X}\right|\right) - \mathrm{a\,tan}\left(\left|\frac{B_y}{B_x}\right|\right)\right|$.

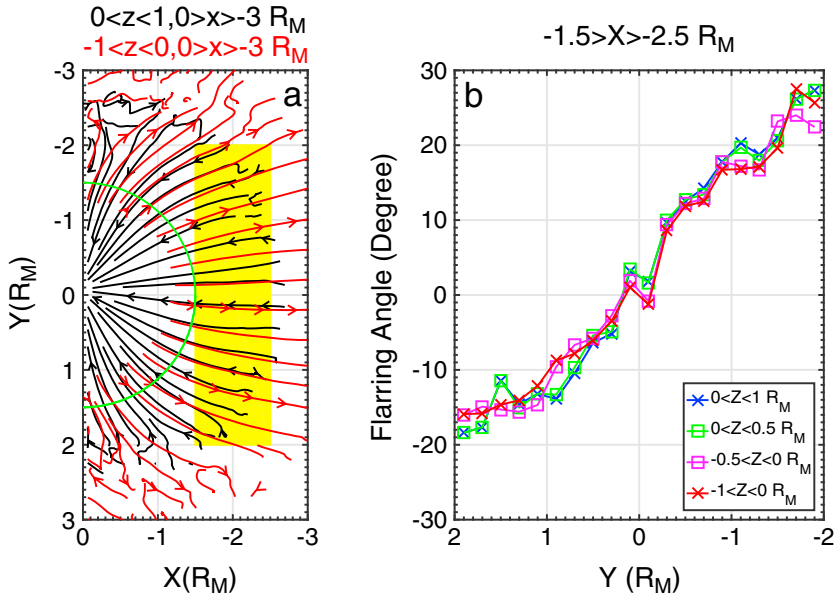


**Figure 6.** (a) The average configuration of magnetic field lines in magnetotail and (b) the variation of flaring angle of field lines against the coordinate of $Y$ with different limits of $Z$ ranges.

Since the $Z$ range at northern hemisphere can be measured up to $Z = 1\ R_M$ (see Figure 3), the two ranges $|Z| < 0.5\ R_M$ and $|Z| < 1\ R_M$ are surveyed here to check the possible variation along $Z$ coordinates. Based on the average values of $B_x$ and $B_y$ component in the $X$-$Y$ plane, the average deviation angle $\Delta\alpha$ and the magnetic field lines of the two $Z$ ranges are calculated and shown in Figure 5.

Figures 5a and 5c show the distribution of $\Delta\alpha$ for $|Z| < 0.5\ R_M$ and $|Z| < 1\ R_M$, respectively. It is clear that no matter what the $Z$ range is, within the radial distance about 1.5 $R_M$ (see the green hemi-circle in both panels), the field lines are almost radially orientated. In contrast, the field lines evidently deviate from the radial direction beyond the radial distance about 1.5 $R_M$. Thus, the radial distance about 1.5 $R_M$ should be the transition location from the dipole field to the magnetotail. We also note from Figure 5c that near the point ($X = 0$, $Y = 0$), the deviation angle increases significantly. Several possible reasons can account for it: (1) the actual dipole center is not strictly located at the point of ($X = 0$, $Y = 0$); (2) the magnetic axis is not strictly along the $Z$ axis of coordinates, and (3) the field lines from the polar cap are connected with the stretched lobe field; thus, the deviation might be associated with the impact of external magnetospheric currents.

Figures 5b and 5d show the average field lines for $|Z| < 0.5\ R_M$ and $|Z| < 1\ R_M$, respectively. It is clear from both panels that the average field lines in the northern hemisphere ($Z > 0$, black curves with arrow) and southern hemisphere ($Z < 0$, red curves with arrow) of magnetotail are flaring with respect to the plane of $Y = 0$, showing the consistence with the distribution of $B_y$ in Figures 4d–4f.

To describe the flaring of MFLs (magnetic field lines) in magnetotail quantitatively, it is helpful to define the flaring angle as the angle between magnetic field vector and the plane of $Y = 0$. We select the region $-1.5 < X < -2.5$ and $|Y| < 2\ R_M$ (the yellow-shaded region in Figure 6a) to calculate to flaring angles to probe the field structure of magnetotail current sheet. The reasons for selecting the region are that (1) the radial distance about 1.5 $R_M$ can be seen as the boundary from the dipole field to the magnetotail (see Figures 5a and 5c) and (2) the measurements of tail field at northern hemisphere can only reach up to $X = -2.5\ R_M$ (see Figure 3) due to the bias of orbit coverage. The range of $|Y| < 2\ R_M$ is divided into 20 bins with step 0.2 $R_M$. In each bin, the flaring angle can be calculated as atan($B_y/B_x$) and the ratio $B_y/B_x$ is calculated by the linear regression from the scattering plots of $B_x$ component versus $B_y$ component in that bin.

Figure 6b shows the variation of flaring angle against with the $Y$ coordinate when considering the limit $0 < Z < 1\ R_M$ (blue-cross line), $0 < Z < 0.5\ R_M$ (green-square line), $-0.5 < Z < 0$ (magenta-square line), and $-1 < Z < 0\ R_M$ (red-cross line), respectively. These limits yield almost the same variation profile.

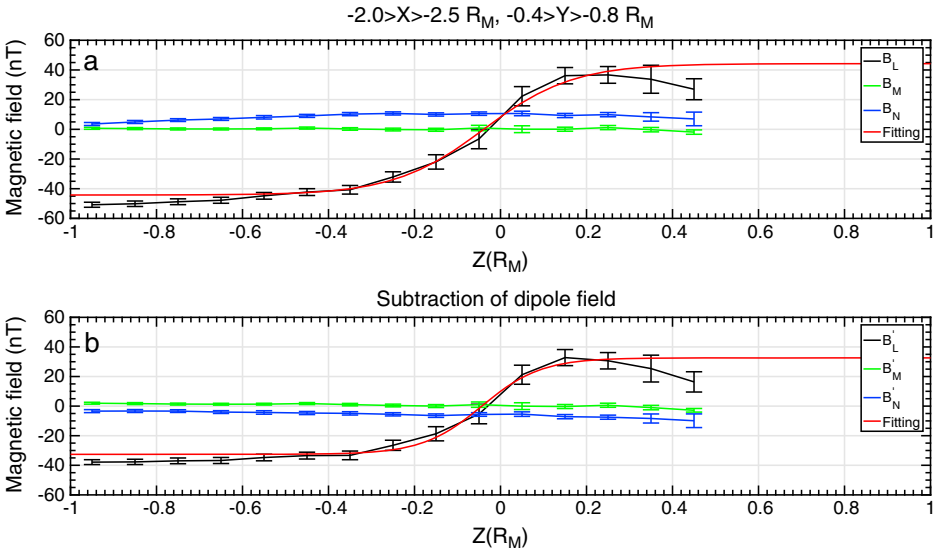


**Figure 7.** (a) The distribution of magnetic field components over a local current sheet ($0 < Y < 0.5\ R_M$ and $-2 > X > -2.5\ R_M$). (b) The distribution when the dipole field is subtracted. The red line in both panels is the Harris fitting of $B_L$ component. The length of error bar represents the 95% confidence interval.

Clearly, at the duskside ($Y > 0$) the flaring angle is negative, but positive at the dawnside ($Y < 0$). Figure 6b demonstrates that the field lines are more flared at the dawnside ($Y < 0$) than that at the duskside ($Y > 0$). The reason for the dawn-dusk asymmetry is currently unclear; it may suggest that the tail current is dawn-dusk asymmetric. It is also interesting to note that the flaring angle range is basically the same as that found in the Earth magnetotail with downstream distance 20–33 $R_E$ (Fairfield, 1979).

### 3.4. Characteristics of Tail Current Sheet

#### 3.4.1. Example of Calculating Curvature Radius and Current Density

In this section, we will quantitatively estimate the characteristics of magnetotail current sheet, including the curvature radius of field lines and the current density. To estimate these parameters, one has to check the profile of magnetic field over current sheet. Before starting to check the profile, it is helpful to define a local coordinate of current sheet. In this coordinates, $\hat{\mathbf{L}}$ is along the lobe field direction pointing planetward, $\hat{\mathbf{N}}$ is the same as the $+Z$ direction (it can be seen as the normal of the current sheet, we will show it in the later analysis), and $\hat{\mathbf{M}} = \hat{\mathbf{N}} \times \hat{\mathbf{L}}$ completes the right-handed coordinate system. Since the flaring angle of MFLs can be evaluated, $\hat{\mathbf{L}}$ can be computed as $\hat{\mathbf{L}} = \hat{\mathbf{x}}\cos\alpha + \hat{\mathbf{y}}\sin\alpha$, where $\hat{\mathbf{x}}$ and $\hat{\mathbf{y}}$ are the unit vectors along $+X$ and $+Y$ directions, while $\alpha$ is the average flaring angle of field lines.

As an example, an average profile of magnetic field over current sheet with all orbits' measurements within the region $-2.0 > X > -2.5\ R_M$ and $-0.4 < Y < -0.8\ R_M$ is shown in Figure 7. In this example, the average flaring angle is estimated as 9.4°; thus, we can derive $\mathbf{L}$ = [0.99, 0.16, 0], and $\mathbf{M}$ = [−0.16, 0.99, 0] in the frame of MSM coordinates. Accordingly, the corresponding magnetic field components $B_L$, $B_M$, and $B_N$ along these directions can be obtained. Figure 7a shows the profiles of these components over $|Z| < 1\ R_M$ (the range of $-1 < Z < 1\ R_M$ is divided into 20 bins for the average calculation). The lengths of the error bars are $2 \times 1.96\frac{\sigma}{\sqrt{n}}$, representing the 95% confidence interval, where $\frac{\sigma}{\sqrt{n}}$ is the standard error of the mean, $n$ is the data number in that bin. The $B_L$ component varies significantly over the CS. We fit the $B_L$ component to a Harris sheet model $B_L = B_0 \tanh\left(\frac{Z-Z_0}{L_0}\right)$ (Harris, 1962), where $B_0$ is the lobe field, $L_0$ is the typical sheet scale, and $Z_0$ is the shift of sheet center. The fit is shown as a red line, and the fitting parameters are given in Table 1. In contrast to the $B_L$ component, the $B_N$ component (the normal component) is approximately constant over current sheet, it is about 10.6 nT at the reversal of $B_L$, while the $B_M$ component is negligible over the whole range. Thus, the current sheet can be well seen as 1-D sheet. The minimum curvature

**Table 1**
*The Estimated Parameters of Mercury's Tail Current Sheet in the Region Within $-2 > X > -2.5\ R_M$ and $-0.4 > Y > -0.8\ R_M$*

| | $B_M$[a] (nT) | $B_N$[a] (nT) | $Z_0$[b] ($R_M$) | $B_0$[b] (nT) | $L_0$[b] ($R_M$) | $R_{c,min}$[c] (km) | Adjusted $R$ square[d] |
|---|---|---|---|---|---|---|---|
| Original data set | 0.71 | 10.60 | $-0.04 \pm 0.04$ | $44.25 \pm 5.71$ | $0.21 \pm 0.09$ | $123 \pm 61$ | 0.97 |
| | $B_M^{'}$[a] (nT) | $B_N^{'}$[a] (nT) | $Z_0$[b] ($R_M$) | $B_0$[b] (nT) | $L_0$[b] ($R_M$) | $J_0$[c] (nA/m$^2$) | Adjusted $R$ square[d] |
| Subtraction of dipole field | 0.05 | −6.69 | $-0.04 \pm 0.04$ | $32.60 \pm 5.49$ | $0.14 \pm 0.09$ | $76 \pm 45$ | 0.95 |

[a]The value interpolated at the sheet center. [b]The fitted parameters from Harris sheet model with 95% confidence bounds. [c]$R_{c,min}$ and $J_0$ are the estimated magnetic field curvature radius and current density, respectively, at CS center based on Harris sheet fitting. [d]The coefficient of adjusted $R$ square indicates the fitting goodness; i.e., the more closer to one it is, the better the fit would be.

radius of MFLs at current sheet center ($B_L = 0$) can be estimated as $R_{c,\min} = \frac{B_N L_0}{B_0}$ (Büchner & Zelenyi, 1989) and tabulated in Table 1. Based on the fitting error of parameters, the error of $R_{c,\ \min}$ can be evaluated as $\Delta R_{c,\min} = \sqrt{\left(\frac{\partial R_{c,\min}}{\partial B_0}\right)^2 \Delta B_0^2 + \left(\frac{\partial R_{c,\min}}{\partial L_0}\right)^2 \Delta L_0^2}$.

If current sheet is 1-D, $R_{c,min}$ can represent the half-thickness of neutral sheet, which is defined as the span with $|B_L| < B_N$ over $B_L = 0$ along the normal direction (Rong et al., 2010; Shen et al., 2007). The current density at the sheet center, in principal, can be computed as $j_0 = \mu_0^{-1} \frac{dB_L}{dz}\Big|_{z=z_0} = \frac{B_0}{\mu_0 L_0}$ via the Harris fitting; nonetheless, the observed $B_L$ contains the contribution from dipole field, which is unrelated with the current density. Thus, to accurately evaluate the current density, one has to remove the dipole field.

Accordingly, after removing the dipole field based on the estimated dipole moment by Anderson et al. (2011), the average flaring angle of the remnant magnetic field is estimated as 8.6°. We repeat the same procedures to construct the local coordinates for the remnant magnetic field and plot the profile of magnetic field components in Figure 7b. To differentiate with $B_L$, $B_M$, and $B_N$, the $L$, $M$, and $N$ components of the remnant field are labeled as $B_L^{'}$, $B_M^{'}$, and $B_N^{'}$, respectively. Again, we find that the $B_L^{'}$ component can be well fitted by the Harris model, while the $B_N^{'}$ component is approximately constant over CS (it is about −6.7 nT at the reversal of $B_L^{'}$), and the $B_M^{'}$ component is negligible. The current density at sheet center, $J_0$, can be reasonably evaluated in this case, and the estimated value is tabulated in Table 1. The error of $J_0$ can be evaluated as $\Delta J_0 = \sqrt{\left(\frac{\partial J_0}{\partial B_0}\right)^2 \Delta B_0^2 + \left(\frac{\partial J_0}{\partial L_0}\right)^2 \Delta L_0^2}$. The curvature radius is not calculated because it makes no sense to estimate it when dipole field is removed.

Consequently, from Table 1 in this case, we find that the profile of $B_L$ component can be well fitted by the Harris model no matter the dipole field is removed or not, and the calculated curvature radius of MFLs and the current density at the current sheet center are $R_{c,min}$ = 123 km and $J_0$ = 76 nA/m$^2$, respectively. Our result is also consistent with the study of Poh et al. (2017a), which estimated the median cross-tail current density in the current sheet to be 78 nA/m$^2$ to each identified current sheet crossing.

### 3.4.2. Cross-Tail Current Sheet Structure

Since the tail current sheet is well covered by MESSENGER within $-1.5 > X > -2.5\ R_M$, the calculation can also be conducted in the yellow-shaded region of Figure 6a to survey the distributions of $R_{c,min}$ and $J_0$. To look for a possible variation of the distribution along $X$ direction, the $X$ range is divided into two regions: the inner tail ($-1.5 > X > -2.0\ R_M$) and the outer tail ($-2.0 > X > -2.5\ R_M$). The range of $Y$ ($-2\ R_M > Y > 2\ R_M$) is divided into 10 sectors with width 0.4 $R_M$, and the $Z$ coordinate is confined to $|Z| < 1\ R_M$. Repeating the same procedures as applied in section 3.4.1, the $R_{c,min}$ and $J_0$ in these regions of tail current sheet are derived, which are tabulated in Tables 2 and 3.

From Table 2, it is clear that the whole surface of the surveyed current sheet center is located at the equatorial plane ($Z_0 = 0$); thus, the $+Z$ direction or $\hat{\mathbf{N}}$ can be well seen as the normal of current sheet. We also find that the normal component $B_N$ (the average of $B_N$ is about 15 nT in inner tail, and 10 nT in outer tail) is much larger than the cross-tail component $B_M^{'}$ which demonstrates that the plane of MFLs is basically vertical to the equatorial plane, and the current sheet can be well approximated to be 1-D sheet. The coefficient of the "adjusted $R$ square" (>0.90) indicates that the $B_L$ component can be well fitted by the Harris model in the whole surveyed current sheet except for the regions near $|Y| = 2\ R_M$.

**Table 2**
*The Estimated Parameters of Mercury's Tail Current Sheet*

| $X$ ($R_M$) | $Y$ ($R_M$) | $B_M$ (nT) | $B_N$ (nT) | $Z_0$ ($R_M$) | $B_0$ (nT) | $L_0$ ($R_M$) | $R_{c,min}$ (km) | Adjusted $R$ square | $\alpha$ (deg) |
|---|---|---|---|---|---|---|---|---|---|
| −1.5 to −2.0 | −2 to −1.6 | −1.32 | 19.42 | −0.04 ± 0.09 | 30.29 ± 11.00 | 0.38 ± 0.31 | 594 ± 531 | 0.8882 | 28.6 |
| | −1.6 to −1.2 | −1.32 | 19.53 | −0.05 ± 0.03 | 51.72 ± 8.48 | 0.54 ± 0.17 | 498 ± 177 | 0.9880 | 20.3 |
| | −1.2 to −0.8 | 0.49 | 17.31 | −0.03 ± 0.03 | 58.19 ± 5.42 | 0.44 ± 0.09 | 319 ± 72 | 0.9924 | 18.3 |
| | −0.8 to −0.4 | 0.20 | 17.67 | −0.03 ± 0.03 | 71.94 ± 8.98 | 0.45 ± 0.13 | 270 ± 85 | 0.9572 | 13.4 |
| | −0.4–0 | −0.60 | 16.70 | −0.01 ± 0.01 | 73.93 ± 3.97 | 0.39 ± 0.05 | 215 ± 30 | 0.9967 | 4.7 |
| | 0–0.4 | 0.85 | 14.85 | −0.01 ± 0.03 | 80.33 ± 8.32 | 0.46 ± 0.11 | 207 ± 54 | 0.9898 | −2.6 |
| | 0.4–0.8 | 0.48 | 15.79 | −0.01 ± 0.02 | 69.37 ± 5.16 | 0.41 ± 0.08 | 228 ± 48 | 0.9934 | −9.4 |
| | 0.8–1.2 | −0.35 | 12.97 | −0.01 ± 0.02 | 53.67 ± 3.46 | 0.38 ± 0.06 | 224 ± 38 | 0.9949 | −13.9 |
| | 1.2–1.6 | −0.83 | 13.81 | −0.04 ± 0.02 | 49.07 ± 4.39 | 0.51 ± 0.09 | 350 ± 69 | 0.9958 | −17.0 |
| | 1.6–2.0 | −1.32 | 15.67 | 0.02 ± 0.02 | 32.68 ± 2.55 | 0.46 ± 0.08 | 538 ± 103 | 0.9941 | −19.2 |
| −2.0 to −2.5 | −2 to −1.6 | 1.54 | 12.80 | −0.03 ± 0.04 | 30.74 ± 4.94 | 0.47 ± 0.17 | 478 ± 189 | 0.9705 | 17.3 |
| | −1.6 to −1.2 | −2.90 | 11.96 | −0.03 ± 0.02 | 41.16 ± 3.11 | 0.32 ± 0.06 | 227 ± 46 | 0.9920 | 15.5 |
| | −1.2 to −0.8 | −4.06 | 11.30 | 0.00 ± 0.03 | 46.67 ± 5.21 | 0.37 ± 0.1 | 219 ± 64 | 0.9830 | 11.7 |
| | −0.8 to −0.4 | 0.71 | 10.60 | −0.04 ± 0.04 | 44.24 ± 5.71 | 0.21 ± 0.10 | 123 ± 61 | 0.9666 | 9.4 |
| | −0.4–0 | 1.45 | 8.27 | 0.00 ± 0.02 | 51.93 ± 3.39 | 0.28 ± 0.05 | 109 ± 21 | 0.9932 | 4.0 |
| | 0–0.4 | 0.21 | 7.73 | −0.01 ± 0.01 | 49.7 ± 1.73 | 0.26 ± 0.03 | 99 ± 12 | 0.9979 | 0.6 |
| | 0.4–0.8 | 1.21 | 10.03 | 0.01 ± 0.01 | 48.59 ± 2.20 | 0.29 ± 0.04 | 146 ± 21 | 0.9968 | −4.5 |
| | 0.8–1.2 | 0.02 | 8.78 | 0.03 ± 0.03 | 46.56 ± 5.50 | 0.42 ± 0.10 | 193 ± 51 | 0.9832 | −8.9 |
| | 1.2–1.6 | 0.24 | 9.99 | −0.01 ± 0.03 | 39.44 ± 4.88 | 0.42 ± 0.12 | 260 ± 81 | 0.9836 | −9.4 |
| | 1.6–2.0 | −0.42 | 12.94 | 0.07 ± 0.07 | 25.8 ± 6.38 | 0.26 ± 0.20 | 318 ± 257 | 0.8076 | −11.2 |

*Note*. The format is the same as that in Table 1 except for the last column added as the average flaring angle of magnetic field.

Figure 8a shows the distribution of the $B_N$ component against the $Y$ coordinate for the inner tail (blue line) and outer tail (red line). The $B_N$ component in the inner tail is stronger than that in the outer tail, which is reasonable since the inner tail is closer to the planet. Interestingly, to note that, particularly in the inner tail, $B_N$ is stronger at the dawnside than that at the duskside, showing evident dawn-dusk asymmetry.

Figure 8b shows the distributions of the derived $R_{c,min}$. Being consistent with Figure 8a, for the inner tail, the profile of $R_{c,min}$ shows some dawn-dusk asymmetry, the minimum plateau of $R_{c,min}$ (about 200 km) is

**Table 3**
*The Estimated Parameters of Mercury's Tail Current Sheet After the Subtraction of Dipole Field*

| $X$ ($R_M$) | $Y$ ($R_M$) | $B'_M$ (nT) | $B'_N$ (nT) | $Z_0$ ($R_M$) | $B_0$ (nT) | $L_0$ ($R_M$) | $J_0$ (nA/m$^2$) | Adjusted $R$ square | $\alpha$ (deg) |
|---|---|---|---|---|---|---|---|---|---|
| −1.5 to −2.0 | −2 to −1.6 | −1.40 | 6.50 | −0.02 ± 0.12 | 19.90 ± 8.04 | 0.29 ± 0.33 | 22.38 ± 27 | 0.8183 | 27.8 |
| | −1.6 to −1.2 | −1.17 | 1.01 | −0.06 ± 0.03 | 34.71 ± 4.68 | 0.49 ± 0.13 | 23.10 ± 7 | 0.9896 | 15.6 |
| | −1.2 to −0.8 | 0.51 | −8.36 | −0.03 ± 0.03 | 34.27 ± 3.00 | 0.34 ± 0.08 | 32.87 ± 8 | 0.9892 | 14.0 |
| | −0.8 to −0.4 | 0.21 | −13.44 | −0.03 ± 0.03 | 38.89 ± 3.86 | 0.36 ± 0.10 | 35.23 ± 10 | 0.9874 | 10.6 |
| | −0.4–0 | −0.57 | −18.99 | −0.01 ± 0.01 | 38.06 ± 1.19 | 0.31 ± 0.03 | 40.04 ± 4 | 0.9984 | 3.7 |
| | 0–0.4 | 0.85 | −20.95 | 0.00 ± 0.02 | 42.60 ± 3.33 | 0.39 ± 0.08 | 35.62 ± 8 | 0.9921 | 0.2 |
| | 0.4–0.8 | 0.48 | −15.09 | −0.01 ± 0.02 | 38.31 ± 2.41 | 0.32 ± 0.06 | 39.04 ± 8 | 0.9929 | −4.0 |
| | 0.8–1.2 | −0.40 | −12.43 | −0.01 ± 0.02 | 32.05 ± 1.68 | 0.28 ± 0.05 | 37.33 ± 7 | 0.9949 | −7.5 |
| | 1.2–1.6 | −1.50 | −5.31 | −0.05 ± 0.03 | 33.57 ± 4.39 | 0.47 ± 0.13 | 23.29 ± 7 | 0.9888 | −11.1 |
| | 1.6–2.0 | −1.24 | 1.87 | 0.03 ± 0.03 | 23.48 ± 2.51 | 0.42 ± 0.10 | 18.23 ± 5 | 0.9866 | −15.2 |
| −2.0 to −2.5 | −2 to −1.6 | 1.65 | 3.28 | −0.04 ± 0.05 | 24.65 ± 4.67 | 0.44 ± 0.19 | 18.27 ± 9 | 0.9536 | 16.5 |
| | −1.6 to −1.2 | −2.83 | 0.58 | −0.03 ± 0.03 | 32.94 ± 2.85 | 0.28 ± 0.07 | 38.37 ± 10 | 0.9881 | 14.1 |
| | −1.2 to −0.8 | −4.07 | −2.64 | 0.00 ± 0.04 | 35.88 ± 4.37 | 0.33 ± 0.10 | 35.46 ± 12 | 0.9770 | 10.5 |
| | −0.8 to −0.4 | 0.05 | −6.69 | −0.04 ± 0.04 | 32.62 ± 4.48 | 0.14 ± 0.08 | 75.99 ± 45 | 0.9532 | 8.6 |
| | −0.4–0 | 1.45 | −10.14 | 0.00 ± 0.02 | 38.17 ± 2.16 | 0.23 ± 0.04 | 54.12 ± 10 | 0.9938 | 3.5 |
| | 0–0.4 | 0.19 | −10.69 | −0.01 ± 0.01 | 36.37 ± 1.56 | 0.21 ± 0.03 | 56.48 ± 8 | 0.9962 | 2.2 |
| | 0.4–0.8 | 1.25 | −6.31 | 0.01 ± 0.01 | 36.49 ± 1.86 | 0.25 ± 0.04 | 47.60 ± 8 | 0.9951 | −2.6 |
| | 0.8–1.2 | 0.18 | −5.89 | 0.04 ± 0.04 | 35.73 ± 5.26 | 0.37 ± 0.13 | 31.49 ± 12 | 0.9691 | −6.8 |
| | 1.2–1.6 | 0.31 | −1.44 | −0.01 ± 0.03 | 30.90 ± 3.96 | 0.37 ± 0.11 | 27.24 ± 9 | 0.9792 | −7.1 |
| | 1.6–2.0 | 0.22 | 3.20 | $0.05 \pm 6.36 \times 10^{13}$ | 18.31 ± 4.47 | $0.01 \pm 8.97 \times 10^{13}$ | - | 0.7867 | −10.5 |

*Note*. The format is the same as that in Table 2 except that the column of $R_{c,min}$ is replaced by $J_0$.

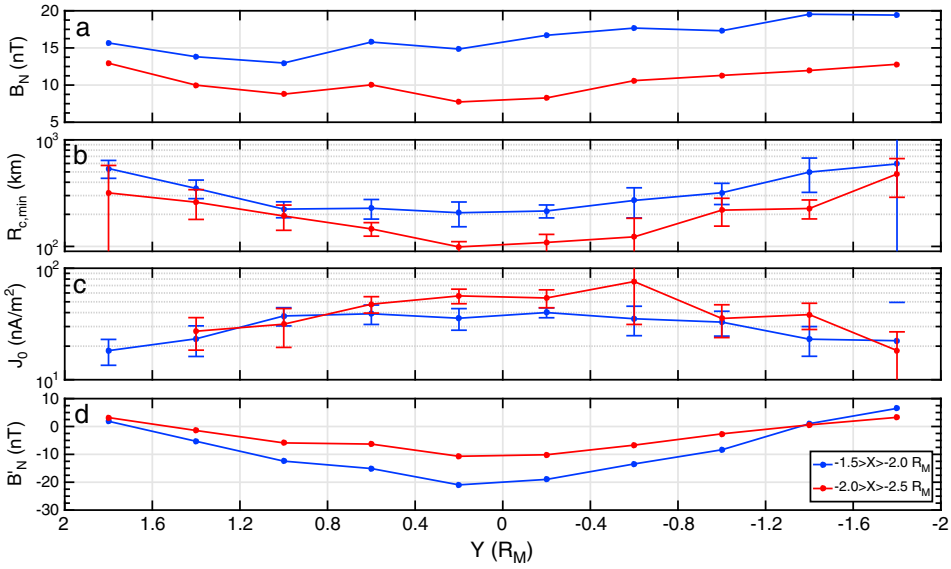


**Figure 8.** Panels from top to bottom show the distribution of the normal component of magnetic field, the curvature radius of field lines at the current sheet center, the current density at the sheet center, and the normal component of magnetic field after the subtraction of dipole field. In all panels, the blue line is for the inner tail ($-1.5 > X > -2.0\ R_M$), while the red line is for the outer tail ($-2.0 > X > -2.5\ R_M$). The length of error bar represents the 95% confidence interval.

concentrated in $-0.4 < Y < 1.2\ R_M$, and increases toward both flanks (500–600 km). In contrast, in outer tail, the profile of $R_{c,min}$ is of less dawn-dusk asymmetry, and the values are correspondingly smaller than that in the inner tail. $R_{c,min}$ reaches the minimum around midnight about 100 km and increases up to 400 km at both flanks. Thus, it suggests that the field lines are more stretched in the outer tail.

Table 3 lists the fitted parameters after the subtraction of dipole field. Again, the coefficient of the adjusted $R$ square (>0.90) indicates that the Harris fitting is very well except for the regions near both flanks. We find that even the dipole field is removed, the current sheet center is still located at the equatorial plane. The normal component $B'_N$ becomes negative, but the magnitude is still much larger than the cross-tail component $B'_M$, which indicates that the current sheet only associated with the tail current can also be well seen as 1-D sheet.

Figure 8c shows the distribution of the current density $J_0$ when dipole field is removed. Being consistent with the profile of $R_{c,min}$ in the inner tail, the profile of $J_0$ in the inner tail also shows a dawn-dusk asymmetry; i.e., $J_0$ reaches a maximum plateau (about 40 nA/m$^2$) around $-0.4 < Y < 1.2\ R_M$ and decreases near both flanks (about 20 nA/m$^2$). By comparison, in the outer tail, the values of $J_0$ are correspondingly larger than that in the inner tail. $J_0$ is about 50 nA/m$^2$ around the midnight and decreases down to about 20 nA/m$^2$ near both flanks. It is a little surprised that $J_0$ jumps to 76 nA/m$^2$ for $-0.4 > Y > -0.8\ R_M$ in the outer tail (the different size of the $Z$ range also yields the comparable $J_0$ in this region). Due to its larger error bar, we would rather attribute it to the calculation error. Note that due to the very large fitting error, the $J_0$ in the $1.6 < Y < 2.0$ $R_M$ of the outer tail is not tabulated in Table 3; thus, it is also missed in Figure 8c.

Figure 8d show the distribution of the $B'_N$ component when dipole field is removed. The negative $B'_N$ is associated with the duskward cross-tail current. From Figure 8d, we find that the magnitude of the negative $B'_N$ reaches the maximum around midnight, and it is larger in the inner tail than that in the outer tail. It is reasonable because the implied $\frac{\partial B'_N}{\partial Y} < 0$ ($\frac{\partial B'_N}{\partial Y} > 0$) at $Y < 0$ ($Y > 0$) suggests that the tail current density has component $j_x < 0$ ($j_x > 0$) at $Y < 0$ ($Y > 0$), and the implied $\frac{\partial B'_N}{\partial X} < 0$ suggest that the current density has component $j_y > 0$. The implications of the gradient of $B'_N$ are not surprising, because the direction of cross-tail current is nearly perpendicular to the local lobe field direction. Thus, the cross-tail current $J_0$ must have $+j_y$ and $-j_x$ component at dawnside, while $+j_y$ and $+j_x$ component at the duskside. Thus, the profile of $B'_N$ consistently suggests that the cross-tail current is azimuthally flowing from the dawn to the dusk. Near both flanks, $B'_N$ becomes minor positive, which could be related with the magnetopause current, because the

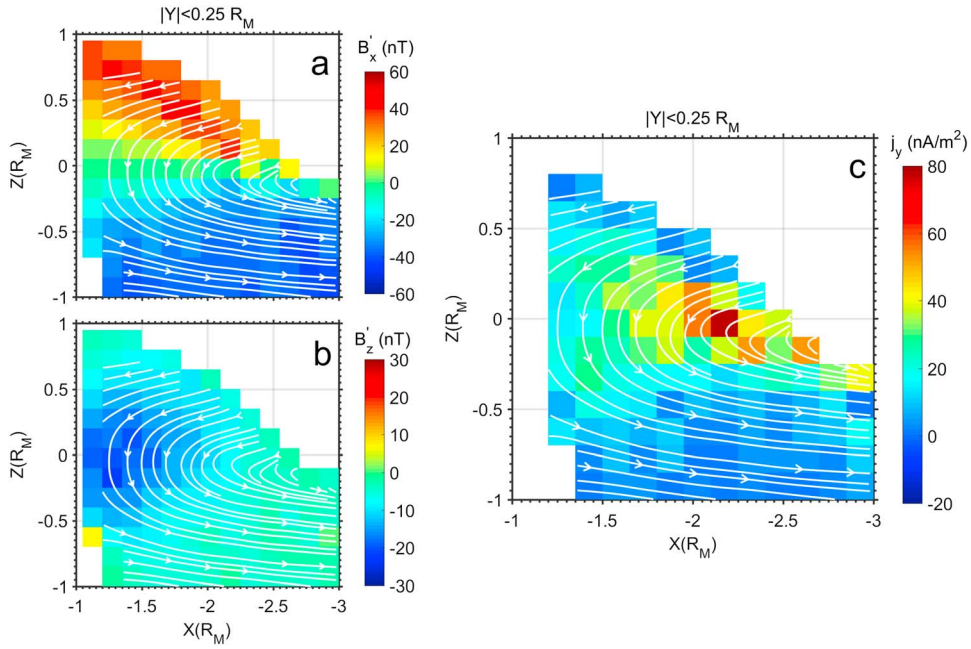


**Figure 9.** (a and b) The distribution of $B_x$ and $B_z$ component in the *X-Z* plane after the subtraction of the dipole field and (c) the distribution of *Y* component of current density $j_y$. The white lines in these panels represent the average field lines after the subtraction of dipole field.

magnetopause current at the dawnside (duskside) flank is supposed flowing sunward (tailward), which can induce the positive $B_N'$ inside the magnetosphere.

### 3.4.3. 2-D Distribution of Tail Current Density

In the above section, the current density is only modeled at the sheet center with restriction of $|Z| < 1\ R_M$. Here with the spatial distribution of magnetic field, the curl of magnetic field $\nabla \times \mathbf{B}$ can be computed, so that the spatial distribution of current density in magnetotail can be derived. Again, to calculate the current density, the dipole field has to be removed from the magnetic field measurements as that has been done in Figure 7b, that is $\mathbf{B}' = \mathbf{B} - \mathbf{B}_{\text{dipole}}$, where $\mathbf{B}'$ is the remnant field, $\mathbf{B}$ is the recorded magnetic field, and $\mathbf{B}_{\text{dipole}}$ is the dipole field based on the dipole moment estimated by Anderson et al. (2011). The *x*, *y*, and *z* components of $\mathbf{B}'$ are labeled as $B_x'$, $B_y'$, and$B_z'$respectively.

Here without loss generality, we survey the spatial distribution of the cross-tail current near midnight where the current is nearly along *Y* direction. Figures 9a and 9b show a cut of the distribution of $B_x'$ component and $B_z'$ component, respectively, in the *X-Z* plane around midnight ($|Y| < 0.25\ R_M$). The *Y* component of current density, $j_y$, can be approximately calculated as $j_y \approx \mu_0^{-1}\left(\frac{\Delta B_x'}{\Delta Z} - \frac{\Delta B_z'}{\Delta X}\right)$, and Figure 9c displays the distribution of the derived $j_y$. In these panels, the *X-Z* plane ($2\ R_M \times 2\ R_M$) is partitioned into $20 \times 20$ bins, and the superimposed white lines represent the average MFLs of remnant field, $\mathbf{B}'$.

At least, three new features are noted in Figure 9c: (1) The cross-tail current around midnight is basically concentrated in $|Z| < 0.25\ R_M$, which demonstrates that the half-thickness of current sheet is about $0.25\ R_M$ (600 km), much larger than the curvature radius $R_{c,\min}$ (100–200 km) at the sheet center (or the half-thickness of neutral sheet). The half-thickness is also consistent with the sheet scale, $L_0$ as shown in Table 3. (2) The tail current density is significant at $X < -1.5\ R_M$. In other word, the inner edge of tail current sheet around midnight is located about $X = -1.5\ R_M$, showing the well agreement with the flaring angle distribution from Figures 5a and 5c. The distributions of $j_y$ in the *X-Z* plane with other ranges of *Y* coordinate also show the similar features (not shown here). (3) The spatial distribution of $j_y$ near $X = -1.5\ R_M$ shows a bifurcated structure; the enhanced $j_y$ near the inner edge can intrude into the high latitude of both hemispheres.

It is worthy to note that the half-thickness of tail current sheet and the edge location have been determined by Johnson et al. (2012) using the MAG data from 24 March to 12 December 2011 when constructing their

magnetospheric model. In their study, the half-thickness is determined based on the rotation of field vector over the current sheet. They found that the field rotation is 95% complete within 140 km (0.06 $R_M$) of current sheet center and approach its asymptotic value at a distance of 350 km (0.14 $R_M$).Thus, they set the half-thickness to be 0.09 $R_M$, with a lower and upper bound of 0.06 and 0.14 $R_M$, respectively. Since the curvature radius indicates the spatial scale of the rotation, the half-thickness reported by Johnson et al. (2012) is comparable to the curvature radius in current sheet as we find here (see Figure 8b), which is smaller than the half-thickness as we defined here from the Harris fitting (see the value of "$L_0$" in Table 3).

As to the inner edge location of current sheet, Johnson et al. (2012) identified 47 crossings of equatorial plane in the near-tail region without plasma sheet characteristics after substraction of dipole field and obtained the mean radial distance to these equator crossings to be 1.41 $R_M$, which was considered as the distance to the inner edge of the cross-tail current sheet. The inner edge location estimated by Johnson et al. (2012) is consistent with our study though they did not address the current distribution directly. The recent study by Poh et al. (2017a) showed the $\delta B_z$ distribution against $X$ coordinates within the current sheet, where $\delta B_z$ is the magnetic field after the removal of the dipole field component and assumes the magnetic field contribution from the Chapman-Ferraro current at Mercury's magnetopause to be negligible. They modeled the Mercury's current sheet using a simple "slab" model, fit the model results to the downtail variation of $\delta B_z$, and found a local minimum of the $B_z$ at $X \sim -1.22$ $R_M$, which was determined to be the location of the inner edge of the current sheet. Our result is consistent with that derived in Poh et al. (2017b). The small difference in the location of the inner edge of the current sheet between both studies could be due to the difference in identification method of Mercury's current sheets. In our study, all magnetic field data points from all orbits are binned and averaged while the study of Poh et al. (2017b) identified current sheet crossings and its boundaries using a set of criteria and only perform further analysis on magnetic field measurements of current sheet crossings with acceptable fits to the Harris current sheet model.

## 4. Discussion

The average morphology or Mercury's magnetotail with down tail less than 3 $R_M$ is statistically surveyed by the measurements of magnetometer onboard MESSENGER. In this section, parts of the results are discussed in comparison with the knowledge of Earth's magnetotail.

### 4.1. Shape of Tail Magnetopause

The distribution of magnetic field in the *Y-Z* plane (see Figure 4) shows that the scale of magnetotail along *Z* direction is significantly larger than that along the *Y* direction. In other words, the tail magnetopause is significantly elongated along the south-north direction. This finding is a bit surprising, because most Earth magnetospheric models cannot show such feature (certainly, some models actually had assumed the cylindrical shape of magnetotail), even in the state-of-art 3-D asymmetric model (Lin et al., 2010).

Such feature has been recently noticed by Zhong, Wan, Slavin, et al. (2015) in their 3-D asymmetric magnetopause model for Mercury though it might be associated with the orbital bias due to fewer magnetopause crossings sampled at the nightside.

Although the existence of this feature is definitely confirmed by our study, the reason for the presence of tail elongation in the north-south direction is still an open issue. Here we try to present possible reasons based on the following analysis:

1. The theoretical analysis by Mead and Beard (1964) demonstrates that the interaction between dipole field and the unmagnetized solar wind would yield a magnetotail of cylindrical shape. Thus, the elongation is probably related with the IMF in solar wind, or alternatively with the uneven interaction. Simulations about Earth magnetotail suggested that the magnetotail could be elongated along the IMF orientation when projected in the *Y-Z* plane, particularly during the period of low-solar-wind Alfvénic Mach number (e.g., Ridley, 2007; Sibeck & Lin, 2014). Nonetheless, statistically speaking, the orientation of IMF should conform to the Parker-spiral pattern and lie in ecliptic plane. Thus, the elongation along the south-north direction cannot be the result of IMF effect; otherwise, the elongation is along the dawn-dusk direction. Readers are suggested to refer to the discussions of Zhong, Wan, Slavin, et al. (2015, and references therein). As a result, the uneven interaction might be the reason to explain the elongation. The uneven interaction of Mercury's magnetosphere with solar wind is understandable, because the north shift of

the dipole center favors the high latitude of southern hemisphere being directly exposed to the shocked solar wind according to the asymmetric model of Zhong, Wan, Slavin, et al. (2015). In other words, the solar wind energy could be absorbed directly by the surface of Mercury at the high latitude of southern hemisphere. The absorption makes the dipole field "feel" reduced compression by solar wind in the high latitude of southern hemisphere, so that it induces the inflation of magnetosphere along the south-north direction. In a word, we may argue that the north shift of the dipole center can account for the elongation of magnetotail along south-north direction.

2. The other possible reason is associated with induction currents in Mercury's interior. Mariner 10 estimates of Mercury's mass implied a metallic core with radius 72–90% of the planetary radius, i.e., about 2,000 km (Harder & Schubert, 2001; Hauck et al., 2007). The standoff distance of Mercury's magnetopause is about 1.5 $R_M$, or ~3,600 km (e.g., Winslow et al., 2013; Zhong, Wan, Slavin, et al., 2015). The closeness of the magnetopause to Mercury's surface results in induction currents being driven on the surface of the core when the solar wind pressure changes (Glassmeier et al., 2007; Hood & Schubert, 1979). These inductive currents resist changes in the planetary magnetic field and "stiffen" the field lines rooted in Mercury's interior. In other words, the inductive effect fixes the foot points of field lines, and even the open field lines of Mercury from polar cap are not as easily deformed by the solar wind as is the case of Earth. Consequently, the "stiff" field lines emanating from Mercury's polar cap might make the magnetotail elongated along the south–north direction.

It is uncertain which explanation is reasonable; further simulations are needed to check the validity of these hypotheses.

### 4.2. Magnetospheric Scaling to Earth

Considering the average standoff distance of the magnetopause ($R_{ss}$ = 1.5 $R_p$ for Mercury and $R_{ss}$ = 11 $R_p$ for Earth; $R_p$ is the planetary radius), morphologically speaking, the Mercury's magnetosphere is roughly a factor of 8 smaller than that of Earth's, as normalized by the planetary radius. By the same simple scaling, the surveyed region of Mercury' magnetotail with down tail less than 3 $R_M$ is equivalent to be Earth's magnetotail with down tail less than 20 $R_E$ (Earth radius, $R_E$ = 6,371 km).

Based on the multipoint analysis of Cluster in the Earth's magnetotail at a distance 15–19 $R_E$, Rong et al. (2011) estimated that the half-thickness of neutral sheet is about 0.3 $R_E$ around the midnight and 1.2 $R_E$ at both flank regions. In other words, the thickness of neutral sheet near flanks is about four times the thickness of that around midnight. The magnetospheric scaling suggests that the down tail 15–19 $R_E$ of Earth's magnetotail is roughly corresponded to the down tail 2–2.5 $R_M$ of Mercury's magnetotail. Our calculations in this scope find that the half-thickness of neutral sheet (or $R_{c,min}$) is about 0.04 $R_M$ (about 100 km) around the midnight and about 0.16 $R_M$ (about 400 km) at both flanks, which consistently shows the neutral sheet at both flanks is just four times as thick as that around midnight.

Meanwhile, it is interesting to note that the half-thickness of neutral sheet in the Mercury's magnetotail is just a factor of 8 smaller than that in the Earth's, which demonstrates the well consistence with the scaling of the two magnetospheres (Ogilvie et al., 1977).

### 4.3. Dawn-Dusk Variation

The observations of Earth magnetotail within down tail 10–20 $R_E$ show that the Earth magnetotail has a dawn-dusk asymmetry. The curvature radius of MFLs in current sheet is found smaller around the midnight and the duskside with stronger cross-tail current density, which favors the dynamic process, e.g., magnetic reconnections occurred more frequently there (e.g., Genestreti et al., 2014; Nagai et al., 2013; Nagai et al., 2015; Rong et al., 2010; Rong et al., 2011; Rong et al., 2014; Slavin et al., 2005). The fast flows in the near-Earth magnetotail are also strongly localized in the local time sector 21:00–01:00 (McPherron et al., 2011). Vlasova et al. (2002) and Walsh et al. (2014) summarized the characteristics of the dawn-dusk asymmetry. However, the reasons for the asymmetry are unclear. Simulation suggests that the asymmetry is regulated by the spatial variation in ionospheric conductance and would disappear when the conductance is spatially uniform (Zhang et al., 2012).

In Figure 8, our calculations show that the $B_N$ component and the curvature radius of MFLs in current sheet indeed display similar dawn-dusk asymmetry; that is, both $B_N$ and curvature radius are smaller in the

duskside. The asymmetry is prominent in the inner tail but less significant in the outer tail ($-2.0 > X > -2.5$ $R_M$). Thus, it seems that the dawn-dusk asymmetry just localizes in the Mercury's magnetotail.

Being contrary to the asymmetry of magnetic field distribution, previous study showed that the tail activities, e.g., flux ropes and dipolarization fronts, tend to appear in the dawnside (Sun et al., 2016). In other words, the distribution of thinner current sheet does not show the correspondence to the distribution of tail activities, which is different to the case of Earth's magnetotail. Therefore, the mechanism to control the dawn-dusk asymmetric profile of magnetic field of Mercury's magnetotail should be different with that of the Earth's magnetotail. One possible reason to explain the dawn-dusk asymmetry of magnetic field of Mercury's magnetotail is the dawn-dusk asymmetric distribution of heavy ions. The numerical simulations by Delcourt et al. (2003) showed that the energetic $Na^+$ inclines to move to the dusk flank of magnetotail when particles are launched on the noon meridian (see their Figure 2), which can result in a dawn-dusk asymmetric distribution of $Na^+$ density (see their Figure 4) with a density accumulation in the dusk flank. Raines et al. (2013) observed that the $Na^+$-group ions are indeed enhanced in the premidnight sector. Due to the diamagnetic effect of the charged particles in magnetic field, it is reasonable to infer that the dawn-dusk asymmetric distribution of heavy ions can account for the asymmetric distribution of magnetic field. We note that the recent study by Poh et al. (2017b) also consistently attributed the asymmetry to the preferred appearance of heavy ions on the duskside. However, being different from the diamagnetic effect we suggested here, they argued that "…The mass loading of energetic heavy ions from the NMNL and cusp increases the thermal plasma pressure duskside of the current sheet, resulting in stretching (weaker $B_Z$) and thinning of the duskside current sheet…".

## 5. Summary

Using the MESSENGER's magnetic field data during 2011–2015, the average magnetic field structure of Mercury's magnetotail is statistically studied within the downstream distance 0–3 $R_M$. The derived results can be summarized as follows:

1. Mercury has a terrestrial-like magnetotail. The magnetic field lines, emanating from the southern hemisphere, are significantly stretched in the nightside. A cross-tail current sheet is present in the equatorial plane, which separates the lobes of antiparallel field lines.
2. The cross section of magnetotail in *Y-Z* plane is not circular. The scale of magnetotail along *Z* direction is about 5 $R_M$, but along the *Y* direction is about 4 $R_M$. Thus, the shape of magnetotail is elongated along the south-north direction. In *X-Z* plane, the size of magnetotail increases with the downstream distance and the field lines near the southern boundary of magnetotail deviate from *X* axis about 14°.
3. The typical field strength in lobe is about 50 nT, and the open magnetic flux in lobe is estimated to be about $2.3 \times 10^6$ Wb, which implies that the polar cap latitude for the northern hemisphere (southern hemisphere) should be higher (lower) than 37°.
4. In tail current sheet, the normal component of magnetic field, $B_N$ ($B_N$ is about 15 nT in inner tail, and about 10 nT in outer tail), is much larger than the cross-tail component, $B_M$ ($B_M$ is about zer0). Thus, the magnetotail current sheet can be well seen as 1-D sheet.
5. The magnetic field in magnetotail is flaring with respect to the midnight ($Y = 0$). In the dawnside, the $B_y$ component is positively proportioned with the $B_x$ component, while it is negatively correlated in the duskside. Inside radial distance about 1.5 $R_M$, the field lines are basically orientated along the radial direction as projected on the *X-Y* plane, but deviated significantly from the radial direction beyond 1.5 $R_M$.
6. The magnetotail current sheet can be well fitted by the Harris sheet model. The fitting results show that the average curvature radius of MFLs at the sheet center is smaller around the midnight (about 200 km for inner tail and 100 km for the outer tail) but with stronger current density (about 40 nA/m$^2$ for inner tail and 50 nA/m$^2$ for the outer tail). While the curvature radius increases toward both flanks (500–600 km for inner tail and about 400 km for outer tail) with the decreased current density (about 20 nA/m$^2$ for both inner tail and outer tail).
7. The typical half-thickness of tail current sheet around the midnight is about 0.25 $R_M$ (about 600 km), and the inner edge of current sheet is located about $X = -1.5$ $R_M$. The cross-tail current flows azimuthally from the dawn to the dusk.
8. The magnetic field structure in magnetotail has a dawn-dusk asymmetry: In comparison with the dawnside ($Y < 0$), in the duskside ($Y > 0$), the field lines are less flaring, the normal component of magnetic

field in current sheet is weaker, and the curvature radius of field lines in current sheet is smaller. The dawn-dusk asymmetry is prominent in the inner tail ($-2.0 > X > -2.5\ R_M$), but less significant in the outer tail ($-2.0 > X > -2.5\ R_M$). The asymmetry is probably induced by the diamagnetic effect of the enhanced planetary heavy ions in the premidnight sector.

We should remind that the observation characteristics revealed above just draw the average morphology of Mercury's magnetotail. Many factors, which is ignored in our study, e.g., substorm processes, IMF, dynamic pressure of solar wind, and dipole tilt angle (though minor), can actually impact the magnetic field structure of magnetotail. Thus, many related issues are worthy to be pursued in the future with the baseline of this study.

Additionally, the estimated curvature radius $R_{c,min}$ in tail current sheet is an important parameter to evaluate the adiabaticity of charged particle, which is determined by $\kappa = \sqrt{R_{c,\min}/\rho_{\max}}$, where $\rho_{max}$ is the maximum gyroradius of particle (e.g., Büchner & Zelenyi, 1989; Sergeev et al., 1983).If $\kappa \gg 1$, the particle motion is adiabatic. As $\kappa$ decreases toward unity, the particle motion becomes stochastic and nonadiabatic (Büchner & Zelenyi, 1989; Delcourt et al., 1996; Sergeev et al., 1983). It was also suggested that the thermal electrons with $\kappa \cong 1$ would favor the tearing mode instability or the onset of disruption of current sheet (Büchner & Zelenyi, 1989; Pulkkinen et al., 1994). The dynamics of charged particle in Mercury's tail current sheet will be addressed further in a future study combining the derived $R_{c,min}$ and the plasma measurements by FIPS.

We hope that our study can also benefit the Mercury's magnetosphere models (e.g., Alexeev et al., 2008; Johnson et al., 2012; Korth et al., 2015) for the further refinement.

## Appendix A: The Calculation of Polar Cap Latitude

In section 3.2, the open flux of polar cap is estimated to be $\Phi \approx 2.3 \times 10^6$ Wb. Taking account of the previously estimated dipole moment 195 nT × $R_M^3$ by Anderson et al. (2011), the average polar cap latitude can be calculated.

As shown in Figure A1, in the geographic coordinates, the original point O is at the planetary center, the arbitrary point **r** at the surface of Mercury is **r** ($R_M \sin\theta \cos\varphi$**i**, $R_M \sin\theta \sin\varphi$**j**, $R_M \cos\theta$**k**), where $R_M$ is the Mercury's radius, $\theta$ is the polar angle, $\varphi$ is the azimuth angle. The dipole center is at $\mathbf{r}_0$ (0**i**, 0**j**, $d$**k**) where $d$ is the shifted distance of dipole center along $Z$ axis.

For the ideal dipole field, the magnetic field radial component is

$$B_r = \frac{-M}{\Delta r^3}\cos\theta', \tag{A1}$$

where $M$ is the magnetic field strength at the equatorial plane of planetary surface, $\Delta r$ is the radial distance of point **r** to the dipole center, and $\theta'$ is the polar angle with respect to the dipole center.

From Figure A1, it is easy to derive $\Delta\mathbf{r} = \mathbf{r} - \Delta\mathbf{r}_0 = (R_M \sin\theta \cos\varphi\mathbf{i}, R_M \sin\theta \sin\varphi\mathbf{j}, R_M \cos\theta - d\mathbf{k})$, and

$$\cos\theta' = \frac{\Delta\mathbf{r}\cdot\hat{\mathbf{z}}}{|\Delta\mathbf{r}|} = \frac{R_M\cos\theta - d}{\sqrt{R_M^2\sin^2\theta + (R_M\cos\theta - d)^2}} \tag{A2}$$

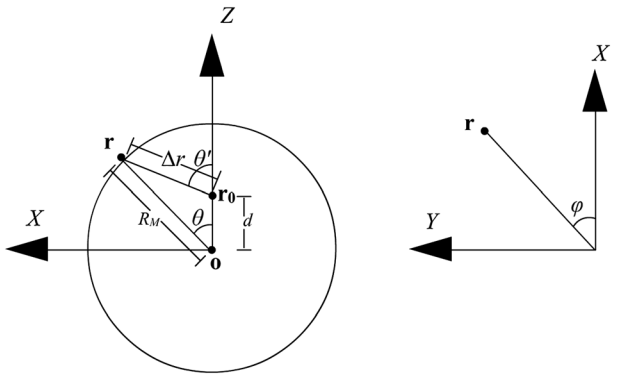


**Figure A1.** Sketched diagram to show the situation when dipole center is shifted along $Z$ direction.

Combining equations (A1) and (A2), the open magnetic flux at northern hemisphere can be calculated as

$$\begin{aligned}\Phi &= \int_0^{\theta_0}\int_0^{2\pi} B_r R_M^2 \sin\theta\, d\theta\, d\varphi \\ &= -2\pi M R_M^2 \int_0^{\theta_0} \frac{R_M\cos\theta - d}{\left[R_M^2\sin^2\theta + (R_M\cos\theta - d)^2\right]^2}\sin\theta d\theta\end{aligned} \tag{A3}$$

Considering $M = 195 \times R_M^3$ nT and $d \approx 0.198\ R_M$ (Anderson et al., 2011), and the estimated open flux $\Phi \approx 2.3 \times 10^6$ Wb, the polar angle of polar cap is estimated to be $\theta_0 \approx 50°$. Thus, the polar cap latitude at northern hemisphere is about 40°.

Similarly, the calculation of open magnetic flux at southern hemisphere via

$$\Phi = -2\pi M R_M^2 \int_{\theta_0}^{\pi} \frac{R_M \cos\theta - d}{\left[R_M^2 \sin^2\theta + (R_M \cos\theta - d)^2\right]^2} \sin\theta d\theta, \tag{A4}$$

yields the polar angle of polar cap $\theta_0 \approx 124°$. Thus, the polar cap latitude at southern hemisphere is about 34°.

The shift distance $d$ equals zero; that is, dipole center is coincidentally with planetary center. In this case, the average polar cap latitude is roughly 37° from equation (A3).

**Acknowledgments**
We are thankful to the MESSENGER MAG team for providing the magnetic field data. The MAG data used in this paper is available from the Planetary Data System (http://ppi.pds.nasa.gov/). This work is supported by the National Natural Science Foundation of China (grants 41374180, 41525016, 41321003, 41621063, 41231066, and 41774188), the National Postdoctoral Program for Innovative Talents (grant BX201600158), and the China Postdoctoral Science Foundation (grant 2016M600124).

## References

Alexeev, I. I., Belenkaya, E. S., Bobrovnikov, S. Y., Slavin, J. A., & Sarantos, M. (2008). Paraboloid model of Mercury's magnetosphere. *Journal of Geophysical Research*, *113*, A12210. https://doi.org/10.1029/2008JA013368

Alexeev, I. I., Belenkaya, E. S., Slavin, J. A., Korth, H., Anderson, B. J., Baker, D. N., … Solomon, S. C. (2010). Mercury's magnetospheric magnetic field after the first two MESSENGER flybys. *Icarus*, *209*, 23–39. https://doi.org/10.1016/j.icarus.2010.01.024

Anderson, B. J., Acuña, M. H., Korth, H., Purucker, M. E., Johnson, C. L., Slavin, J. A., … McNutt, R. L. Jr. (2008). The structure of Mercury's magnetic field from MESSENGER's first flyby. *Science*, *321*, 82–85. https://doi.org/10.1126/science.1159081

Anderson, B. J., Johnson, C. L., Korth, H., Purucker, M. E., Winslow, R. M., Slavin, J. A., … Zurbuchen, T. H. (2011). The global magnetic field of Mercury from MESSENGER orbital observations. *Science*, *333*, 1859–1862. https://doi.org/10.1126/science.1211001

Anderson, B. J., Johnson, C. L., Korth, H., Winslow, R. M., Borovsky, J. E., Purucker, M. E., … McNutt, R. L. Jr. (2012). Low-degree structure in Mercury's planetary magnetic field. *Journal of Geophysical Research*, *117*, E00L12. https://doi.org/10.1029/2012JE004159

Anderson, B. J., Acuña, M. H., Lohr, D. A., Scheifele, J., Raval, A., Korth, H., & Slavin, J. A. (2007). The Magnetometer Instrument on MESSENGER. *Space Science Reviews*, *131*, 417–450. https://doi.org/10.1007/s11214-007-9246-7

Andrews, G. B., Zurbuchen, T. H., Mauk, B. H., Malcom, H., Fisk, L. A., Gloeckler, G., … Raines, J. M. (2007). The energetic particle and plasma spectrometer instrument on the MESSENGER spacecraft. *Space Science Reviews*, *131*, 523–556. https://doi.org/10.1007/s11214-007-9272-5

Baker, D., Pulkkinen, T., Angelopoulos, V., Baumjohann, W., & McPherron, R. (1996). Neutral line model of substorms: Past results and present view. *Journal of Geophysical Research*, *101*(A6), 12,975–13,010. https://doi.org/10.1029/95JA03753

Baker, D. N., Poh, G., Odstrcil, D., Arge, C. N., Benna, M., Johnson, C. L., … Zurbuchen, T. H. (2013). Solar wind forcing at Mercury: WSA-ENLIL model results. *Journal of Geophysical Research: Space Physics*, *118*, 45–57. https://doi.org/10.1029/2012JA018064

Baumjohann, W., Hesse, M., Kokubun, S., Mukai, T., Nagai, T., & Petrukovich, A. (1999). Substorm dipolarization and recovery. *Journal of Geophysical Research*, *104*(A11), 24,995–25,000. https://doi.org/10.1029/1999JA900282

Boardsen, S. A., Sundberg, T., Slavin, J. A., Anderson, B. J., Korth, H., Solomon, S. C., & Blomberg, L. G. (2010). Observations of Kelvin-Helmholtz waves along the dusk-side boundary of Mercury's magnetosphere during MESSENGER's third flyby. *Geophysical Research Letters*, *37*, L12101. https://doi.org/10.1029/2010GL043606

Büchner, J., & Zelenyi, L. M. (1989). Regular and chaotic charged particle motion in magnetotaillike field reversals: 1. Basic theory of trapped motion. *Journal of Geophysical Research*, *94*(A9), 11,821–11,842. https://doi.org/10.1029/JA094iA09p11821

Delcourt, D. C., Grimald, S., Leblanc, F., Berthelier, J.-J., Millilo, A., Mura, A., … Moore, T. E. (2003). A quantitative model of the planetary Na+ contribution to Mercury's magnetosphere. *Annales Geophysicae*, *21*, 1723–1736.

Delcourt, D. C., & Seki, K. (2006). On the dynamics of charged particles in the magnetosphere of Mercury. *Advances in Geosciences*, *3*, 17–28. https://doi.org/10.1142/9789812707192_0003

Delcourt, D. C., Sauvaud, J.-A., Martin, R. F. Jr., & Moore, T. E. (1996). On the nonadiabatic precipitation of ions from the near-Earth plasma sheet. *Journal of Geophysical Research*, *101*(A8), 17,409–17,418. https://doi.org/10.1029/96JA01006

DiBraccio, G. A., Slavin, J. A., Raines, J. M., Gershman, D. J., Tracy, P. J., Boardsen, S. A., … Solomon, S. C. (2015). First observations of Mercury's plasma mantle by MESSENGER. *Geophysical Research Letters*, *42*(22), 9666–9675. https://doi.org/10.1002/2015GL065805

DiBraccio, G. A., Slavin, J. A., Imber, S. M., Gershman, D. J., Raines, J. M., Jackman, C. M., … Solomon, S. C. (2015). MESSENGER observations of flux ropes in Mercury's magnetotail. *Planetary and Space Science*, *115*, 77–89. https://doi.org/10.1016/j.pss.2014.12.016

Fairfield, D. (1979). On the average configuration of the geomagnetic tail. *Journal of Geophysical Research*, *84*(A5), 1950–1958. https://doi.org/10.1029/JA084iA05p01950

Fujimoto, M., Baumjohann, W., Kabin, K., Nakamura, R., Slavin, J. A., Terada, N., & Zelenyi, L. (2007). Hermean magnetosphere-solar wind interaction. *Space Science Reviews*, *132*(2-4), 529–550. https://doi.org/10.1007/s11214-007-9245-8

Genestreti, K. J., Fuselier, S. A., Goldstein, J., Nagai, T., & Eastwood, J. P. (2014). The location and rate of occurrence of near-Earth magnetotail reconnection as observed by Cluster and Geotail. *Journal of Atmospheric and Solar: Terrestrial Physics*, *121*(Part A), 98–109. https://doi.org/10.1016/j.jastp.2014.10.005

Gershman, D. J., Slavin, J. A., Raines, J. M., Zurbuchen, T. H., Anderson, B. J., Korth, H., … Solomon, S. C. (2014). Ion kinetic properties in Mercury's premidnight plasma sheet. *Geophysical Research Letters*, *41*, 5740–5747. https://doi.org/10.1002/2014GL060468

Gershman, D. J., Raines, J. M., Slavin, J. A., Zurbuchen, T. H., Sundberg, T., Boardsen, S. A., … Solomon, S. C. (2015). MESSENGER observations of multiscale Kelvin-Helmholtz vortices at Mercury. *Journal of Geophysical Research: Space Physics*, *120*, 4354–4368. https://doi.org/10.1002/2014ja020903

Glassmeier, K., Grosser, J., Auster, U., Constantinescu, D., Narita, Y., & Stellmach, S. (2007). Electromagnetic induction effects and dynamo action in the Hermean system. *Space Science Reviews*, *132*, 511–527. https://doi.org/10.1007/s11214-007-9244-9

Harder, H., & Schubert, G. (2001). Sulfur in Mercury's core? *Icarus*, *151*(1), 118–122. https://doi.org/10.1006/icar.2001.6586

Harris, E. G. (1962). On a plasma sheet separating regions of oppositely directed magnetic field. *Nuovo Cimento*, *23*, 115–121. https://doi.org/10.1007/BF02733547

Hauck, S. A. II, Solomon, S. C., & Smith, D. A. (2007). Predicted recovery of Mercury's internal structure by MESSENGER. *Geophysical Research Letters*, *34*, L18201. https://doi.org/10.1029/2007GL030793

Hood, L., & Schubert, G. (1979). Inhibition of solar wind impingement on Mercury by planetary induction currents. *Journal of Geophysical Research*, *84*(A6), 2641–2647. https://doi.org/10.1029/JA084iA06p02641

Johnson, C. L., Purucker, M. E., Korth, H., Anderson, B. J., Winslow, R. M., al Asad, M. M. H., … Solomon, S. C. (2012). MESSENGER observations ofMercury'smagnetic field structure. *Journal of Geophysical Research*, *117*, E00I14. https://doi.org/10.1029/2012JE004217

Johnson, C. L., Philpott, L. C., Anderson, B. J., Korth, H., Hauck, S. A. II, Heyner, D., … Solomon, S. C. (2016). MESSENGER observations of induced magnetic fields in Mercury's core. *Geophysical Research Letters*, *43*, 2436–2444. https://doi.org/10.1002/2015GL067370

Kallio, E., & Janhunen, P. (2003). Solar wind and magnetospheric ion impact on Mercury's surface. *Geophysical Research Letters*, *30*(17), 1877. https://doi.org/10.1029/2003GL017842

Korth, H., Tsyganenko, N. A., Johnson, C. L., Philpott, L. C., Anderson, B. J., Al Asad, M. M., … McNutt, R. L. Jr. (2015). Modular model for Mercury's magnetospheric magnetic field confined within the average observed magnetopause. *Journal of Geophysical Research: Space Physics*, *120*, 4503–4518. https://doi.org/10.1002/2015JA021022

Lin, R. L., Zhang, X. X., Liu, S. Q., Wang, Y. L., & Gong, J. C. (2010). A three-dimensional asymmetric magnetopause model. *Journal of Geophysical Research*, *115*, A04207. https://doi.org/10.1029/2009JA014235

Lui, A. (2003). Cause of magnetospheric substorms. *Plasma Physics and Controlled Fusion*, *45*(6), 841–852. https://doi.org/10.1088/0741-3335/45/6/301

McPherron, R. L., Hsu, T.-S., Kissinger, J., Chu, X., & Angelopoulos, V. (2011). Characteristics of plasma flows at the inner edge of the plasma sheet. *Journal of Geophysical Research*, *116*, A00I33. https://doi.org/10.1029/2010JA015923

Mead, G. D., & Beard, D. B. (1964). Shape of the geomagnetic field solar wind boundary. *Journal of Geophysical Research*, *69*(7), 1169–1179. https://doi.org/10.1029/JZ069i007p01169

Miura, A. (2001). Ballooning instability as a mechanism of the near-Earth onset of substorms. *Space Science Reviews*, *95*(1/2), 387–398. https://doi.org/10.1023/A:1005249915285

Nagai, T., Shinohara, I., Zenitani, S., Nakamura, R., Nakamura, T. K. M., Fujimoto, M., … Mukai, T. (2013). Three-dimensional structure of magnetic reconnection in the magnetotail from Geotail observations. *Journal of Geophysical Research: Space Physics*, *118*, 1667–1678. https://doi.org/10.1002/jgra.50247

Nagai, T., Shinohara, I., & Zenitani, S. (2015). The dawn-dusk length of the X line in the near-Earth magnetotail: Geotail survey in 1994–2014. *Journal of Geophysical Research: Space Physics*, *120*, 8762–8773. https://doi.org/10.1002/2015JA021606

Ness, N. F., Behannon, K. W., Lepping, R. P., Whang, Y. C., & Schatten, K. H. (1974). Magnetic field observations near Mercury: Preliminary results from mariner 10. *Science*, *185*(4146), 151–160. https://doi.org/10.1126/science.185.4146.151

Ness, N. F., Behannon, K. W., Lepping, R. P., & Whang, Y. C. (1975). Magnetic field of Mercury confirmed. *Nature*, *255*(5505), 204–205. https://doi.org/10.1038/255204a0

Ogilvie, K. W., Scudder, J. D., Vasyliunas, V. M., Hartle, R. E., & Siscoe, G. L. (1977). Observations at the planet Mercury by the plasma electron experiment: Mariner 10. *Journal of Geophysical Research*, *82*(13), 1807–1824. https://doi.org/10.1029/JA082i013p01807

Petrukovich, A. A. (2011). Origins of plasma sheet $B_y$. *Journal of Geophysical Research*, *116*, A07217. https://doi.org/10.1029/2010JA016386

Poh, G., Slavin, J. A., Jia, X., DiBraccio, G. A., Raines, J. M., Imber, S. M., … Solomon, S. C. (2016). MESSENGER observations of cusp plasma filaments at Mercury. *Journal of Geophysical Research: Space Physics*, *121*, 8260–8285. https://doi.org/10.1002/2016JA022552

Poh, G., Slavin, J. A., Jia, X., Raines, J. M., Imber, S. M., Sun, W. J., … Smith, A. W. (2017a). Mercury's cross-tail current sheet: Structure, X-line location and stress balance. *Geophysical Research Letters*, *44*, 678–686. https://doi.org/10.1002/2016GL071612

Poh, G., Slavin, J. A., Jia, X., Raines, J. M., Imber, S. M., Sun, W. J., … Smith, A. W. (2017b). Coupling between Mercury and its nightside magnetosphere: Cross-tail current sheet asymmetry and substorm current wedge formation. *Journal of Geophysical Research: Space Physics*, *122*, 8419–8433. https://doi.org/10.1002/2017JA024266

Pulkkinen, T., Baker, D., Mitchell, D., McPherron, R., Huang, C., & Frank, L. (1994). Thin current sheets in the magnetotail during substorms: CDAW 6 revisited. *Journal of Geophysical Research*, *99*(A4), 5793–5803. https://doi.org/10.1029/93JA03234

Raines, J. M., Gershman, D. J., Zurbuchen, T. H., Sarantos, M., Slavin, J. A., Gilbert, J. A., … Solomon, S. C. (2013). Distribution and compositional variations of plasma ions in Mercury's space environment: The first three Mercury years of MESSENGER observations. *118*, 1604–1619. https://doi.org/10.1029/2012JA018073

Ridley, A. J. (2007). Alfvén wings at Earth's magnetosphere under strong interplanetary magnetic fields. *Annales de Geophysique*, *25*(2), 533–542. https://doi.org/10.5194/angeo-25-533-2007

Rong, Z. J., Shen, C., Lucek, E., Balogh, A., & Yao, L. (2010). Statistical survey on the magnetic field in magnetotail current sheets: Cluster observations. *Chinese Science Bulletin*, *55*(23), 2542–2547. https://doi.org/10.1007/s11434-010-3096-5

Rong, Z. J., Wan, W. X., Shen, C., Li, X., Dunlop, M. W., Petrukovich, A. A., … Lucek, E. (2011). Statistical survey on the magnetic structure in magnetotail current sheets. *Journal of Geophysical Research*, *116*, A09218. https://doi.org/10.1029/2011JA016489

Rong, Z. J., Wan, W. X., Shen, C., Petrukovich, A. A., Baumjohann, W., Dunlop, M. W., & Zhang, Y. C. (2014). Radial distribution of magnetic field in Earth magnetotail current sheet. *Planetary and Space Science*, *103*, 273–285. https://doi.org/10.1016/j.pss.2014.07.014

Rong, Z. J., Lui, A. T. Y., Wan, W. X., Yang, Y. Y., Shen, C., Petrukovich, A. A., … Wei, Y. (2015). Time delay of interplanetary magnetic field penetration into Earth's magnetotail. *Journal of Geophysical Research: Space Physics*, *120*, 3406–3414. https://doi.org/10.1002/2014JA020452

Russell, C. T., Baker, D. N., & Slavin, J. A. (1988). The magnetosphere of Mercury. In F. Vilas, C. R. Chapman, & M. S. Matthews (Eds.), *Mercury* (pp. 514–561). Tucson, AZ: University of Arizona Press.

Sergeev, V. A., Sazhina, E. M., Tsyganenko, N. A., Lundblad, J. A., & Soraas, F. (1983). Pitch-angle scattering of energetic protons in the magnetotail current sheet as the dominant source of their isotropic precipitation into the ionosphere. *Planetary and Space Science*, *31*(10), 1147–1155. https://doi.org/10.1016/0032-0633(83)90103-4

Shen, C., Li, X., Dunlop, M., Shi, Q. Q., Liu, Z. X., Lucek, E., & Chen, Z. Q. (2007). Magnetic field rotation analysis and the applications. *Journal of Geophysical Research*, *112*, A06211. https://doi.org/10.1029/2005JA011584

Sibeck, D. G., & Lin, R.-Q. (2014). Size and shape of the distant magnetotail. *Journal of Geophysical Research: Space Physics*, *119*, 1028–1043. https://doi.org/10.1002/2013JA019471

Slavin, J. A., Smith, E. J., Sibeck, D. G., Baker, D. N., Zwickl, R. D., & Akasofu, S.-I. (1985). An ISEE 3 study of average and substorm conditions in the distant magnetotail. *Journal of Geophysical Research*, *90*(A11), 10,875–10,895. https://doi.org/10.1029/JA090iA11p10875

Slavin, J. A. (2004). Mercurys magnetosphere. *Advances in Space Research*, *33*(11), 1859–1874. https://doi.org/10.1016/j.asr.2003.02.019

Slavin, J. A., Tanskanen, E. I., Hesse, M., Owen, C. J., Dunlop, M. W., Imber, S., … Glassmeier, K. H. (2005). Cluster observations of traveling compression regions in the near-tail. *Journal of Geophysical Research*, *110*, A06207. https://doi.org/10.1029/2004JA010878

Slavin, J. A., Krimigis, S. M., Acuña, M. H., Anderson, B. J., Baker, D. N., Koehn, P. L., … Zurbuchen, T. H. (2007). MESSENGER: Exploring Mercury's magnetosphere. *Space Science Reviews*, *131*(1-4), 133–160. https://doi.org/10.1007/sl%201214-007-9154-x

Slavin, J. A., Acuna, M. H., Anderson, B. J., Baker, D. N., Benna, M., Gloeckler, G., … Zurbuchen, T. H. (2008). Mercury's magnetosphere after MESSENGER's first flyby. *Science*, *321*, 85–89. https://doi.org/10.1126/science.1159040

Slavin, J. A., Anderson, B. J., Baker, D. N., Benna, M., Boardsen, S. A., Gloeckler, G., … Zurbuchen, T. H. (2010). MESSENGER observations of extreme loading and unloading of Mercury's magnetic tail. *Science*, *329*, 665–668. https://doi.org/10.1126/science.1188067

Slavin, J. A., Anderson, B. J., Baker, D. N., Benna, M., Boardsen, S. A., Gold, R. E., … Zurbuchen, T. H. (2012). MESSENGER and Mariner 10 flyby observations of magnetotail structure and dynamics at Mercury. *Journal of Geophysical Research*, *117*, A01215. https://doi.org/10.1029/2011JA016900

Slavin, J. A., DiBraccio, G. A., Gershman, D. J., Imber, S. M., Poh, G. K., Raines, J. M., … Solomon, S. C. (2014). MESSENGER observations of Mercury's dayside magnetosphere under extreme solar wind conditions. *Journal of Geophysical Research: Space Physics*, *119*, 8087–8116. https://doi.org/10.1002/2014JA020319

Solomon, S., McNutt Jr, R. L., Gold, R. E., & Domingue, D. L. (2007). MESSENGER mission overview. *Space Science Reviews*, *131*, 3–39. https://doi.org/10.1007/%20s11214-007-9247-6

Sun, W.-J., Slavin, J. A., Fu, S., Raines, J. M., Zong, Q. G., Imber, S. M., … Baker, D. N. (2015). MESSENGER observations of magnetospheric substorm activity in Mercury's near magnetotail. *Geophysical Research Letters*, *42*, 3692–3699. https://doi.org/10.1002/2015GL064052

Sun, W. J., Fu, S. Y., Slavin, J. A., Raines, J. M., Zong, Q. G., Poh, G. K., & Zurbuchen, T. H. (2016). Spatial distribution of Mercury's flux ropes and reconnection fronts: MESSENGER observations. *Journal of Geophysical Research: Space Physics*, *121*, 7590–7607. https://doi.org/10.1002/2016JA022787

Sundberg, T., Slavin, J. A., Boardsen, S. A., Anderson, B. J., Korth, H., Ho, G. C., … Solomon, S. C. (2012). MESSENGER observations of dipolarization events in Mercury's magnetotail. *Journal of Geophysical Research*, *117*, A00M03. https://doi.org/10.1029/2012JA017756

Tsyganenko, N. A., & Fairfield, D. H. (2004). Global shape of the magnetotail current sheet as derived from Geotail and Polar data. *Journal of Geophysical Research*, *109*, A03218. https://doi.org/10.1029/2003JA010062

Vlasova, N. A., Sosnovets, E. N., & Chuchkov, E. A. (2002). A study of long-term strong dawn–dusk asymmetry of the earth's magnetosphere in 1991. *Advances in Space Research*, *30*(10), 2273–2278. https://doi.org/10.1016/S0273-1177(02)80244-7

Walsh, A. P., Haaland, S., Forsyth, C., Keesee, A. M., Kissinger, J., Li, K., … Taylor, M. G. G. T. (2014). Dawn–dusk asymmetries in the coupled solar wind–magnetosphere–ionosphere system: A review. *Annales de Geophysique*, *32*(7), 705–737. https://doi.org/10.5194/angeo-32-705-2014

Winslow, R. M., Johnson, C. L., Anderson, B. J., Korth, H., Slavin, J. A., Purucker, M. E., & Solomon, S. C. (2012). Observations of Mercury's northern cusp region with MESSENGER's Magnetometer. *Geophysical Research Letters*, *39*, L08112. https://doi.org/10.1029/2012GL051472

Winslow, R. M., Anderson, B. J., Johnson, C. L., Slavin, J. A., Korth, H., Purucker, M. E., … Solomon, S. C. (2013). Mercury's magnetopause and bow shock from MESSENGER magnetometer observations. *Journal of Geophysical Research: Space Physics*, *118*, 2213–2227. https://doi.org/10.1002/jgra.50237

Zhang, B., Lotko, W., Brambles, O., Damiano, P., Wiltberger, M., & Lyon, J. (2012). Magnetotail origins of auroral Alfvénic power. *Journal of Geophysical Research*, *117*, A09205. https://doi.org/10.1029/2012JA017680

Zhong, J., Wan, W. X., Wei, Y., Slavin, J. A., Raines, J. M., Rong, Z. J., … Han, X. H. (2015). Compressibility of Mercury's dayside magnetosphere. *Geophysical Research Letters*, *42*, 10,135–10,139. https://doi.org/10.1002/2015GL067063

Zhong, J., Wan, W. X., Slavin, J. A., Wei, Y., Lin, R. L., Chai, L. H., … Han, X. H. (2015). Mercury's three-dimensional asymmetric magnetopause. *Journal of Geophysical Research: Space Physics*, *120*, 7658–7671. https://doi.org/10.1002/2015JA021425